

**Geochemical and Stratigraphic Analysis of the Linnévatnet Sediment Record:  
A Study of Late Holocene Cirque Glacier Activity in Spitsbergen, Svalbard**

**An Honors Paper for the Department of Earth and Oceanographic Science  
By Graham Harper Edwards**

**Bowdoin College, 2014**

**©2014 Graham Harper Edwards**

## Table of Contents

<b>List of Figures and Tables</b> .....	iii
<b>Acknowledgements</b> .....	iv
<b>Author's Note</b> .....	iv
<b>Abstract</b> .....	1
<b>Introduction</b> .....	2
<b>Background</b>	
<i>Setting</i>	
Geological Setting.....	5
Climate.....	6
Linnédalen and Linnévatnet.....	7
Late Pleistocene and Holocene History of Spitsbergen.....	8
<i>Glacial Activity and the Lacustrine Sediment Record</i> .....	10
<b>Methods</b>	
<i>Field Work</i> .....	12
<i>Laboratory and Analytical Methods</i>	
Core and Sediment Preparation.....	15
Geochemistry and Physical Parameters.....	16
Chronostratigraphy.....	17
Thin-Sections.....	18
<b>Results</b>	
<i>Chronostratigraphy</i> .....	20
<i>Visual Stratigraphy</i> .....	22
<i>Geochemistry and Physical Parameters</i>	
Source Sediments.....	26
Geochemical and Physical Profiles of Core D10.5.....	27
<b>Discussion</b>	
<i>Chronostratigraphy</i> .....	29
<i>Sedimentation Rates and Age Depth Model</i> .....	32
<i>Visual Stratigraphy</i> .....	34

<i>Geochemistry and Physical Parameters</i>	
Source Sediment Interpretations.....	40
Comparison of XRF and ICP-MS Profiles.....	41
Sustained Changes in Colorimetric Lightness and Ti/kcps.....	42
Fluctuations in Ti/kcps and K/kcps.....	43
Variations in Fe/kcps and Magnetic Susceptibility.....	46
Variation in Mn/kcps.....	49
<b>Conclusions and Future Work.....</b>	<b>50</b>
<b>References.....</b>	<b>53</b>
<b>Appendices</b>	
<i>A. Additional Figures.....</i>	<i>60</i>
<i>B. Color Figures in Grayscale.....</i>	<i>65</i>

## List of Figures and Tables

Figure 1.....	3
Figure 2.....	5
Figure 3.....	13
Figure 4.....	14
Figure 5.....	16
Figure 6.....	20
Figure 7.....	21
Figure 8.....	23
Figure 9.....	24
Figure 10.....	25
Table 1.....	27
Figure 11.....	29
Figure 12.....	37

## Acknowledgements

I would like to thank my advisor, Peter Lea, and committee members, Rachel Beane and Mike Retelle, for their mentorship, edits, advice, and assistance throughout this process. Thank you to the faculty and staff of the Bowdoin College Department of Earth and Oceanographic Science for everything along the way. I would also like to thank Mike Retelle, Al Werner, and Steve Roof for an incredible trip to Spitsbergen and great mentorship. Thank you to Maxime Debret and the rest of the 2013 Svalbard REU crew for a remarkable field experience, and special thanks to Allie Balter, Nora Richter, Johanna Eidmann, and Josh Solomon for their collaboration and assistance. I also wish to thank Dr. Mike Ketterer for his expertise and generosity. Finally, I would like to thank my family and friends for their advice, edits, support, and tolerance over the course of this and previous undertakings.

Funding for this research was provided by the Grua/O’Connell Research Award. Funding for field and laboratory research with the Svalbard REU over the summer of 2013 was provided by the National Science Foundation (Award Number: 0649006).

**Author’s Note:** The names of geographic sites in Linnédalen, Svalbard, Norway, are presented here in the original Norwegian. The term “dalen” translates to valley, “breen” to glacier, “elva” to river, and “vatnet” to lake.

## Abstract

Morainal and lacustrine sediments in Linnédalen, Spitsbergen, Svalbard, record the fluctuations of a glacier in a currently unglaciated mountain cirque during the Little Ice Age (LIA). The bedrock composition of this cirque and the adjacent Linnédalen valley wall is lithologically distinct from the other bedrock units of the valley, as are the sediments derived from the cirque and carried into proglacial Linnévatnet by meltwater and runoff. This study attempts to reconstruct Late Holocene glacial activity within this cirque from geochemical, physical, and visual stratigraphic variation of the Linnévatnet lacustrine sediment record. A 57-cm lacustrine sediment core (D10.5), collected from the western sub-basin of Linnévatnet in July 2013, was analyzed at a high-resolution for variations in X-Ray Fluorescence (XRF)-measured elemental composition, spectral reflectance, and magnetic susceptibility; and the visual stratigraphy was observed at a microscopic scale. An age-depth model for D10.5 is developed by extrapolating sedimentation rates from dated horizons, measured by  $^{239+240}\text{Pu}$  radionuclide fallout dating and chemostratigraphic enrichment of atmospheric anthropogenic pollutants.

Visual stratigraphy of the sediment record indicates two periods of cirque glacier sediment delivery to Linnévatnet during the LIA (1329-1363 CE and 1816 CE-Present) as well as a period of elevated erosion, perhaps caused by elevated precipitation, apparently during the Medieval Climate Anomaly (MCA; 984-1082 CE). During non-glacial periods, stratigraphic variation in XRF-measured Ti and K appear to be associated with fluctuations in North Atlantic Oscillation (NAO)-regulated precipitation through the Late Holocene. Within the LIA glacial intervals, profiles of XRF-measured Ti and K exhibit decadal-scale variations in sediment geochemistry that may result from advance and retreat of the cirque glacier ice margin or NAO-driven fluctuations in precipitation. Stratigraphic variation in Fe content indicates complex changes in erosional and hydrological processes in Linnédalen associated with MCA precipitation and glacial meltwater, which need to be better characterized. The stratigraphic and geochemical variations in the lacustrine record of the Linnévatnet west basin indicate that both cirque glacier activity and sediment transport in Linnédalen are more sensitive to climatological change than previously thought.

## Introduction

In the context of ongoing climate change, it is important to consider how different regions of the Earth will be altered by both natural and human-induced variations in climate. The Arctic is considered to be among the regions most susceptible to climate change and most likely to be significantly altered by a warming climate (e.g. Ebbesen et al., 2007; Overpeck et al., 1997). A site of particular interest in the study of Arctic change is the Svalbard archipelago, north of Norway at  $\sim 78^{\circ}\text{N}$  (Fig. 1). Given its situation within patterns of ocean circulation, atmospheric circulation, and sea ice fluctuation, the Svalbard archipelago, and particularly its large western island Spitsbergen, is particularly sensitive and susceptible to variations in climate (Fig. 1; Lamb, 1972, 1977). Nearly 60% of the Svalbard archipelago is currently glaciated, but it is clear from historical observations and geological investigations that the vast majority of its glaciers have decreased in extent over the course of the last century (Liestøl, 1993). Furthermore, these glaciers may exhibit the most negative (geodetic) mass balance in the Arctic, and their volume losses constitute a small but nontrivial contribution to ongoing global sea level rise (Nuth et al., 2010). The glaciers of Svalbard are sensitive to climate variations, and it is important to develop a better understanding of how they will continue to change in response to climate changes. One way to gain this insight is by investigating how glaciers have responded to variable climate in the past.

Prior to the last century or so of rising temperatures, the ‘Little Ice Age’ (LIA), beginning in the 13<sup>th</sup> and 14<sup>th</sup> centuries, was characterized by cooler global temperatures and glacial expansion (Grove, 1988). Studies on glacial activity in Spitsbergen during the LIA provide insight into how glaciers responded to changing climate in the Late Holocene, as well as providing context for the last century or more of glacial retreat on Svalbard. Moraines on Spitsbergen associated with the LIA are the furthest advanced and best preserved of the Holocene, indicating that this interval furnished the most favorable conditions for glacial advance in the last 10,000 years (Werner, 1993). Similarly, Holocene glacial maxima during the LIA interval in Spitsbergen are recorded in the lacustrine sediment record (Svendsen and Mangerud, 1997) and in fossil tundra records (Baranowski and Karlén, 1976; Humlum et al., 2005). It is clear that modern climatic conditions are no longer favorable for the persistence of glaciers at their LIA extents,

whereas conditions during the LIA interval were sufficient on Spitsbergen for the greatest glacial extents of the Holocene.

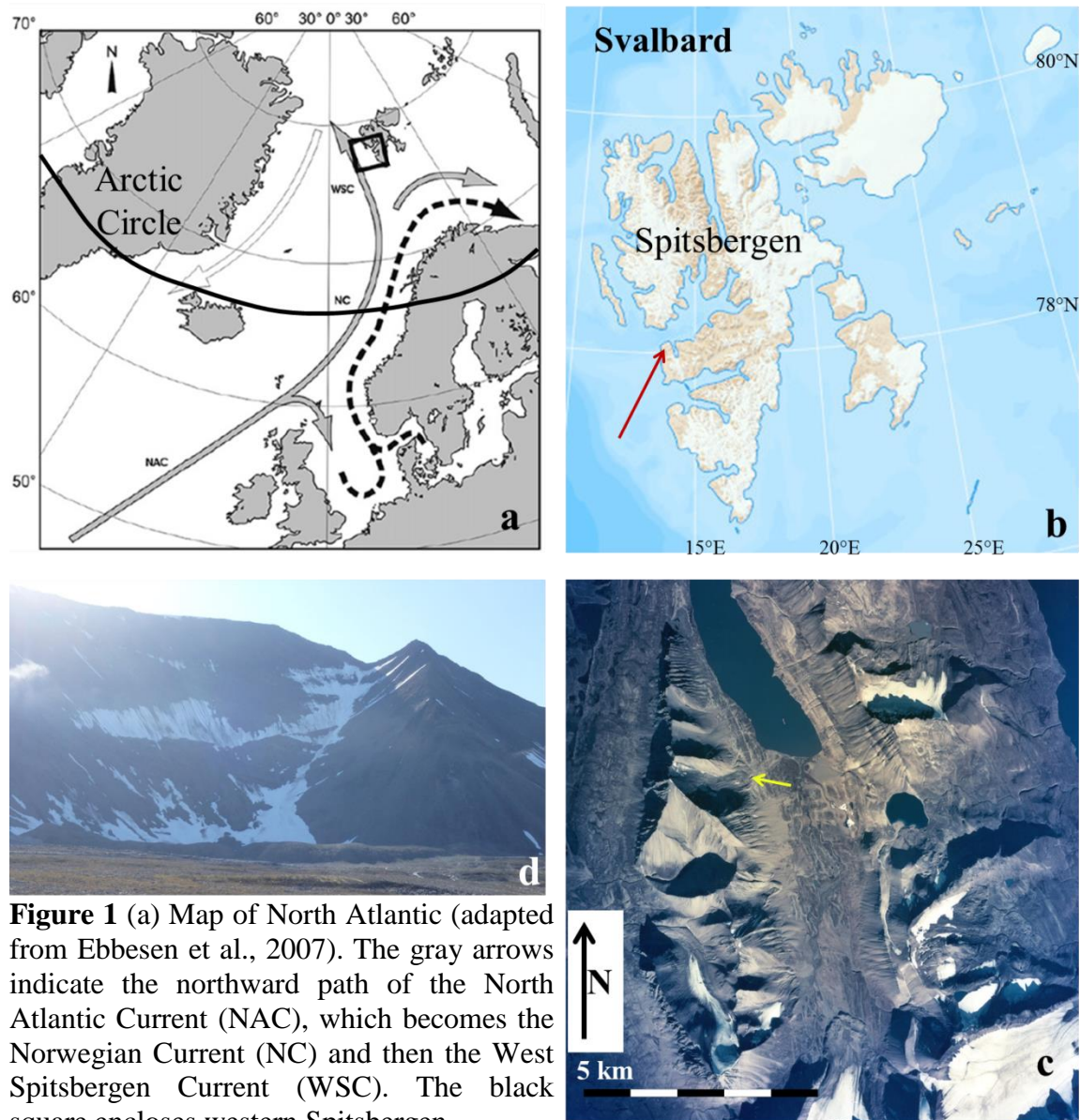


**Figure 1** (a) Map of North Atlantic (adapted from Ebbesen et al., 2007). The gray arrows indicate the northward path of the North Atlantic Current (NAC), which becomes the Norwegian Current (NC) and then the West Spitsbergen Current (WSC). The black square encloses western Spitsbergen.

(b) Map of the Svalbard archipelago with the field site indicated by a red arrow (adapted from [www.toposvalbard.nopolar.no](http://www.toposvalbard.nopolar.no)). (c) Vertical aerial photograph of Linnédalen. Location of west basin cirque is indicated by a yellow arrow (adapted from 1995 aerial photograph; Norsk Polarinstitutt). (d) Photograph of the west basin cirque and moraine. Yellow arrow in (c) indicates position of the photographer.



Of particular interest for this study is evidence in the moraine and lacustrine sediment record for the presence of a small glacier in a currently unglaciated mountain cirque in western Spitsbergen during the LIA interval (Snyder et al., 2000). This specific cirque, referred to henceforth as the “west basin cirque,” occupies the western slopes of Linnédalen, and its meltwater drains into the western sub-basin of the proglacial Linnévatnet (Fig. 1). A unique characteristic of the west basin cirque and the Linnédalen system is that the bedrock unit comprising the western valley wall is distinct from the other bedrock units of the valley (Fig. 2; Hjelle et al., 1986; Ohta et al., 1992). Consequently, glacial sediment from the west basin cirque is expected to be mineralogically distinct from other sediments in the Linnédalen catchment and distinguishable by its lithological and geochemical characteristics.

Snyder et al. (2000) constrained onset of glaciation in the cirque to 400-600 cal. yr BP by inferring glacial activity from the appearance of increased coarse laminae in a sediment core recovered from the west basin of Linnévatnet. The present study attempts to corroborate the findings of Snyder et al. (2000) and additionally reconstruct variations in glacial extent during this interval from the Linnévatnet west basin sediment record using a two-proxy approach. Firstly, the sediment record was analyzed at a microscopic scale and variations in laminae abundance are used as indicators of variations in glacial sediment production and transport. Secondly, this study takes advantage of the distinct west basin cirque lithology and attempts to constrain periods of increased glacial sediment production and transport from the west basin cirque by tracing its geochemical signature through the sediment record, an approach that has been successfully applied to glacial reconstructions of the Canadian Rockies (Leonard, 1986; Leonard and Reasoner, 1999). Cirque glaciers are considered particularly well-suited to provenance studies of glacial activity due to their relatively rapid response times to changes in mass balance (Jansson et al., 2005; Pfeffer et al., 1998). Furthermore, numerous studies (e.g. Karlén and Matthews, 1992; Leonard, 1997; Ohlendorf et al., 1997) have shown that lacustrine sediments can effectively record decadal to century-scale variations in up-valley glacial extent. This study aims to reconstruct such short-term variations in glacier extent during the Late Holocene for the west basin cirque and

provide insight into the dynamics of cirque and small valley glaciers of western Spitsbergen in response to varying climate in the last several centuries.

## Background

### Setting

#### Geologic Setting

Sediments in the Linnédalen system are derived from various rock units that were deposited from the Pre-Cambrian to Mid-Permian. The Hecla Hoek complex includes the various lithostratigraphic groups of the Svalbard basement, and in southwestern Spitsbergen these units are subduction zone metasediments of Precambrian age (Worsley, 2008 & papers cited therein). In upward stratigraphic progression, the basement is overlain by fluvial sandstones and conglomerates of the Billefjorden Group (Upper Devonian and Lower Carboniferous), karstified marine carbonates of the Gipsdalen Group (Mid-Carboniferous to Lower Permian), deep marine carbonates of the Bjarmeland Group, and deep-water fine clastics of the Tempelfjorden and Sassendalen Groups (Mid-Permian; Worsley, 2008). In the mid- to late-Paleogene, compressional dextral strike-slip movement along the Spitsbergen fracture produced folding and thrusting of the bedrock units (Lowell, 1972; Worsley, 2008).

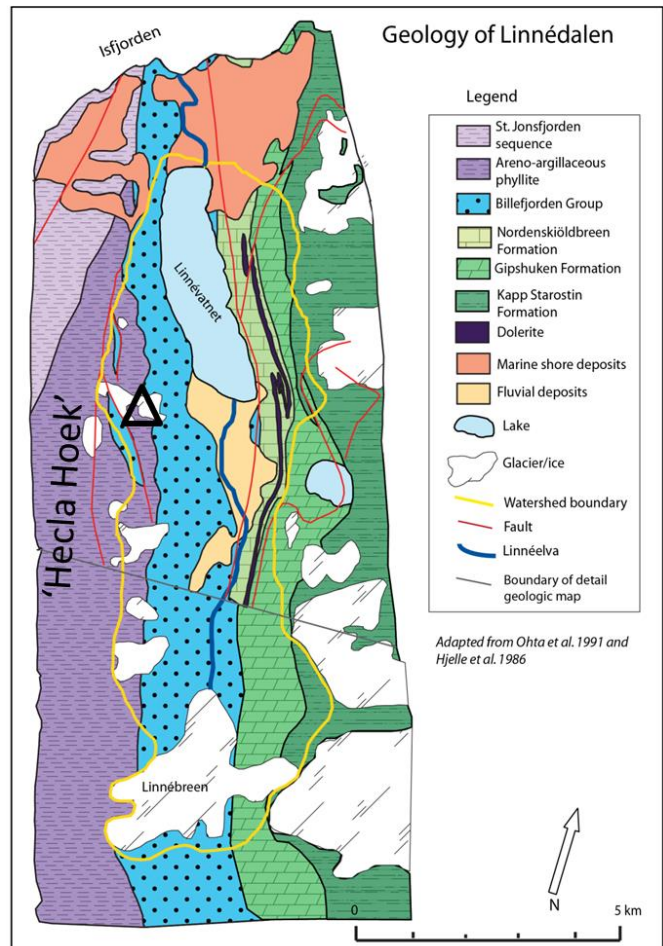


**Figure 2** Bedrock geologic map of Linnédalen. Purple units are the low-grade Lågnabukta metapelites of the Hecla Hoek complex, the blue Billefjorden Group consists of conglomerates and coal-rich sandstones, and the green units are carbonates of the Gipsdalen and Tempelfjorden Groups. A black triangle indicates the location of the west basin cirque. Figure adapted from Perreault (2006).

Linnédalen lies on an E-dipping fold limb associated with Tertiary compressional deformation of Spitsbergen. The upper portion of the western wall of Linnédalen, including the west basin cirque, is comprised of the phyllite-grade Lågneshukta metapelites of the Hecla Hoek complex (Ohta et al., 1992). Lower portions of the western wall, as well as the valley bottom, are comprised of sandstones and conglomerates of the Billefjorden Group (Fig. 2; Hjelle et al., 1986; Ohta et al., 1992). Red sandstones of the lowermost Gipsdalen Group unit, the Petrellskaret Formation, crop out just above lake level at the base of the eastern valley wall (not shown in Fig. 2; Ohta et al., 1992). However, rock units in the eastern valley wall are primarily carbonate rocks of the Gipsdalen Group, with the lowermost formation of the Tempelfjorden Group (Kapp Starosin Fm) occupying the uppermost regions of the valley wall (Fig. 2; Hjelle et al., 1986; Ohta et al., 1992). Dolerite sills associated with Mesozoic volcanism crop out within the carbonate units of the Gipsdalen Group (Fig. 2; Ohta et al., 1992).

## Climate

The Svalbard archipelago (excluding Jan Mayen) lies in the high Arctic between 76°N and 81°N, directly north of Scandinavia (Fig. 1). While the islands of the archipelago exhibit a typical arctic climate, Spitsbergen's proximity to warm Atlantic surface currents results in a considerably warmer and wetter climate than other Svalbard islands and Arctic landmasses of comparable latitude (Svendsen and Mangerud, 1997). Specifically, the West Spitsbergen Current, an extension of the North Atlantic Current, carries warm water ( $>3^{\circ}\text{C}$ ) past the western coast of Spitsbergen (Fig. 1; Swift, 1986). Consequently, mean annual air temperature and precipitation on Spitsbergen's west coast (Isfjord Radio; 78°N, 13°E) have been approximately 6°C warmer and 220 mm higher than on Franz Josef Land (82°N, 52°E) and Thule, Greenland (76°N, 68°W; Lamb, 1972). Instrumental data from the Svalbard Airport in central Spitsbergen provide a mean annual temperature of  $-4.6^{\circ}\text{C}$  and mean annual precipitation of 191 mm for the 1981-2010 time period (Førland et al., 2011).

## Linnédalen and Linnévatnet

A comprehensive description of the Linnédalen system, consistent with field observations from the summer of 2013, is provided by Svendsen et al. (1989), one of a series of papers published on the glacial, sea level, erosional, and lacustrine history of Linnédalen. The bedrock within Linnédalen, below the local marine limit of 70 meters, is covered with a thin, discontinuous layer of muddy marine sediment, overlain by more localized deposits of fluvial, littoral, and talus sediments (Svendsen et al., 1989). The head of Linnédalen is occupied by Linnébreen, a 4-km-long glacier (Figs. 1, 2).

Linnéelva drains the sediment-laden meltwater of Linnébreen into the proglacial Linnévatnet. Linnévatnet is monomictic, isochemical, and isothermal, with annual water temperature below 4°C and ice cover persisting from late September to late July (Bøyum and Kjensmo, 1978 *in* Svendsen et al., 1989). The lake surface is 12 m above modern sea level (a.s.l.). Linnévatnet's north basin is nearly 40 m deep, and eastern and western sub-basins in the southern portion of the lake are both 10-15 m deep and separated by a bathymetric ridge (Svendsen et al., 1989). The north shore of Linnévatnet is bounded by a 30 m a.s.l. marine terrace that separates the lake from marine waters of Isfjorden to the north (Svendsen et al., 1989).

Acoustic profiling of the Linnévatnet floor reveals a basement of bedrock and till, overlain by marine deposits, which are in turn overlain by laminated lacustrine sediments (Svendsen et al., 1989). The lacustrine sediment depth varies from as much as 12m deep near Linnéelva's mouth to less than 2m deep in more distal portions of the basin (Svendsen and Mangerud, 1997). The western sub-basin of Linnévatnet is shielded from the sediment input of Linnéelva by the bathymetric ridge and an overall counterclockwise circulation in the lake; and in result, west basin sediments are considerably thinner and somewhat decoupled from sediments of the east and north basins (Svendsen et al., 1989). The west basin receives the majority of its sedimentary input from the west basin cirque and an associated meltwater stream and fan (Snyder et al., 2000; Svendsen et al., 1989). Additional sediment sources to Linnévatnet and its west basin include steep rivulets on both valley slopes and a snowmelt and groundwater-fed alluvial fan extending from the eastern valley wall (Snyder et al., 2000). Field observations also noted that solifluction

and slumping of valley-bottom sediment, predominantly marine in origin, is a third sediment source to Linnévatnet.

### Late Pleistocene and Holocene History of Spitsbergen

During the last glacial maximum (LGM; Weichselian/Wisconsinan), the Svalbard archipelago was fully glaciated, although some high-altitude regions remained ice-free (Landvik et al., 2003; Landvik et al., 2005). The ice fronts of this glaciation terminated at the edge of the continental shelf, over 40km beyond the present coast of Spitsbergen (Landvik et al., 2005; Svendsen et al., 1992). In Linnédalen, the LGM commenced between 23 and 18  $^{14}\text{C}$  ka BP, with the glacier filling the entire valley and flowing NNW downvalley, terminating north of present-day Linnévatnet (Mangerud et al., 1992).

Deglaciation of Spitsbergen began ca. 14 cal. ka BP and was completed ca. 9  $^{14}\text{C}$  ka BP, accompanied by accelerating rates of landmass emergence (Ebbesen et al., 2007; Forman, 1990; Mangerud et al., 1992; Salvigsen and Høgvard, 2005). Linnédalen, near the western coast of Spitsbergen, deglaciated shortly before 12.3  $^{14}\text{C}$  ka BP, but was a fjord until 9.6  $^{14}\text{C}$  ka BP when isostatic uplift brought the northern terrace above sea level, isolating the upper fjord and creating Linnévatnet as an isolation basin (Mangerud et al., 1992; Mangerud and Svendsen, 1990; Svendsen et al., 1989). The marine sediments blanketing the bedrock of Linnédalen and Linnévatnet were deposited during this 12.3-9.6 ka interval when Linnédalen was still below sea level. The timing of accelerated deglaciation and uplift on Spitsbergen corresponds with a period of significant warmth in the surface waters off of Spitsbergen, driven by a strengthening of the West Spitsbergen Current, which persisted until ca. 8.8 cal. ka BP when the current weakened and cooler conditions persisted until the last two centuries (Ebbesen et al., 2007).

Warm conditions during the Holocene climate optimum persisted in Spitsbergen from ca. 9 to 5.8  $^{14}\text{C}$  ka BP (Blake, 2006; Salvigsen and Høgvard, 2005). This warmth resulted in a period of sustained glacier absence/minima on Spitsbergen, which was followed by reestablishment and readvance of glaciers at high latitudes when conditions cooled (Salvigsen and Høgvard, 2005; Svendsen and Mangerud, 1997). Linnédalen remained fully deglaciated from 11.3 to 5 cal. ka, when Linnébreen began a readvance

that has continued more or less to the present (Svendsen and Mangerud, 1997). However, it was not until the last millennium that the glaciers of Spitsbergen reached their maximum Holocene extents.

The eleventh and twelfth centuries experienced a period of anomalous warmth, predominantly in the Northern Hemisphere, termed the Medieval Climate Anomaly (MCA; Mann et al., 2009). During this period, agriculture and fishing extended further north than ever before in human history and Arctic sea ice was sufficiently reduced to allow Viking landings as far north as 79°N latitude (Jones, 1968; Lamb, 1977). However, the warmth of the MCA was followed in the 13<sup>th</sup> century by the significantly cooler conditions of the LIA (D'Andrea et al., 2012; Mann et al., 2009; Nesje et al., 2008). Conditions during the LIA promoted glacial advance ca. 700 yrs ago, interrupted by a period of relative stagnation or slight retreat, and a final advance to Holocene maximum extents within the last 350 yrs (Grove, 1988). In Spitsbergen, moraines of the late LIA (early-20<sup>th</sup> century stabilization) are the most extensive, while those of earlier LIA (ca. 650 yrs ago) and Neoglacial age are the next most extensive, indicating that LIA advances were the most extensive of the Holocene (Reusche et al., 2014; Werner, 1993). Some evidence suggests that increased winter precipitation, rather than cooler summer temperatures, may have been the dominant driver of the glacial advance in the latter advance of the LIA (D'Andrea et al., 2012; Nesje et al., 2008). Nonetheless, the maximum extent of Linnébreen was reached during the late LIA advance (Svendsen and Mangerud, 1997; Werner, 1993). The findings of Snyder et al. (2000) limit Holocene glacial activity in the west basin cirque to the last 400 years; only during the second, more-extreme LIA period.

The conditions that led to glacial advances in the LIA, however, no longer persist. Since 1840, the Arctic climate has rapidly warmed in response to a number of factors, including volcanic aerosol dissipation, increasing solar radiance, and, more recently, anthropogenic rises in atmospheric trace gases (Overpeck et al., 1997). In the last century, nearly all glaciers on Spitsbergen, including Linnébreen, have retreated in response to climate warming (Werner, 1993). Smaller glaciers on Svalbard currently exhibit large negative mass balances, while larger glaciers, due to either surging behavior or long response times, exhibit relatively stable mass balance in dynamic disequilibrium

(Hagen et al., 2005; Hagen et al., 2003). The west basin cirque has fully deglaciated since its LIA maximum, although final melting may have occurred as late as the mid-20<sup>th</sup> century since a glacier is indicated in topographic maps from the 1930s (Snyder et al., 2000).

### *Glacial Activity and the Lacustrine Sediment Record*

Glacial sediment production and meltwater transport influence lacustrine sedimentation in proglacial lakes, in which evidence of upvalley glacier activity through time may be stored in the sedimentary record. Glaciers effectively generate and erode sediments from bedrock, and this glacial sediment production increases with glacier size and basal area (Jansson et al., 2005). Most glaciers on Svalbard are subpolar, with mixed temperate and non-temperate basal conditions, but the cirque glaciers of Svalbard typically have polar thermal regimes, or non-temperate basal conditions (Björnsson et al., 1996; Hagen et al., 2003; Sverdrup, 1935; Werner, 1993). Jansson et al. (2005) note that while subglacial sediment production processes are less efficient for non-temperate glaciers, basal material can still be deformed and transported. Furthermore, the solely supraglacial drainage of non-temperate glaciers is typically of sufficiently high energy to transport ice-marginal sediments (Hodgkins, 1997). In result, both temperate and polar glaciers effectively generate and transport sediment (Hodgkins, 1997; Jansson et al., 2005). This sediment may then be carried downslope by meltwater streams, and delivered to a proglacial lake, if one is present in the catchment. The accumulation of sediment in proglacial lakes can be significant, as Svendsen et al. (1989) estimated that approximately 50% of the sediment generated by the glaciers in Linnédalen has been deposited in Linnévatnet. Deltas develop as sediment-laden meltwater flows into a lake, and coarser sediments are deposited into proximal zones of the lake basin by turbidity flows or underflows, while more fine-grained sediments remain suspended in the water column and deposit more gradually by settling (Church and Gilbert, 1975). In Linnévatnet, sediment is carried into proximal portions of the basins as underflows, interflows, and overflows, depending on the relative densities of inflowing stream water and ambient lake water, which vary with sediment concentration and temperature (Zamora-Reyes, 2011).

Given this context of glacial sediment generation, transport, and deposition in lacustrine environments, increased glacial extent may be expected to result in increased sedimentation in proglacial lakes. This relationship holds on centurial to millennial timescales, for which long-term variation in glacial extent is reflected in sedimentation rates (Leonard, 1997). Indeed, variation in the Linnévatnet sediment record has been controlled primarily by long-term fluctuations of Linnébreen (Svendsen and Mangerud, 1997). Increased minerogenic sediment production typically occurs with increased glacierized area, while sediment production decreases with glacial retreat (Karlén and Matthews, 1992). In result, high sedimentation rates in proglacial lakes are associated with moraine deposition, including growth and stabilization at glacial maxima, as well as rapid retreat, which exposes previously subglacial sediment to paraglacial erosion (Blass et al., 2003; Karlén and Matthews, 1992; Leonard, 1997).

Several techniques have been applied with success in studies attempting reconstruction of glacial extent and activity from cores of proglacial lacustrine sediment. Based on the direct correlations between glacial activity and lake sedimentation, a particularly effective technique has been inferring sedimentation rates from varve or laminae thicknesses, and using these sedimentological variations as a proxy for variations in upvalley glacial extent (e.g. Leonard, 1997; Ohlendorf et al., 1997; Snyder et al., 2000). For instance, Snyder et al. (2000) inferred late-LIA glaciation in the west basin cirque from the increased frequency of coarse laminae in the Linnévatnet west basin sediment record. In addition to measures of laminae thicknesses, downcore analyses of geochemistry offer potentially informative proxies for increased glacial lake sedimentation in proglacial lakes. In a catchment where carbonate-rich sediments were exclusively glacial in origin, Leonard (1986) and Leonard and Reasoner (1999) used sediment carbonate content as a proxy for glacial activity that closely matched the moraine record. These findings support the potential for using the relative content of compositionally distinct glacial sediment in the lacustrine record as a proxy for upvalley glacial extent. An instrument that shows particular promise for such compositional analyses is the ITRAX Core Scanner. High-resolution (up to 200µm interval) elemental profiles obtained by ITRAX X-Ray Fluorescence (XRF) scans have been used to effectively trace different sediment sources and grain sizes through



lacustrine records from the Canadian Arctic (Cuven et al., 2010, 2011). Another analysis that can measure geochemical and physical properties of lacustrine sediments is magnetic susceptibility (the tendency for a material to magnetize in response to a magnetic field), which increases in lacustrine sediments with increasing content, concentration, and grain size of magnetic minerals (Cohen, 2003). If glacial sediments exhibit a higher magnetic susceptibility, due to either compositional differences or larger grain size, relative glacial sediment contribution may be inferred by this technique. Finally, spectrophotometry used in conjunction with spectrophotometric analysis may be used effectively to define sedimentological units and identify their distribution with high resolution through a sedimentary sequence (Debret et al., 2006; Debret et al., 2011). These various techniques all demonstrate great potential for measuring and developing proxies of historic sedimentological activity, which may in turn be interpreted with respect to upvalley glacial activity.

## **Methods**

### *Field Work*

Field work in Linnédalen was conducted between the 18<sup>th</sup> and 31<sup>st</sup> of July, 2013. Field methods include bathymetric mapping of the Linnévatnet west basin, lacustrine sediment coring, and collection of representative sediments from the Linnédalen watershed. Prior to coring, the bathymetry of the Linnévatnet west basin was mapped by systematically travelling over the area in a tight zig-zag pattern with a bathymeter (Humminbird Echosounder) collecting continuous depth data (Fig. 3). Based on west basin bathymetry, cores were collected from three locations in the west basin: core “Proximal” (abbreviated “P”) was collected proximal to shore and cirque drainage inflow, core “Distal 10.5m” (abbreviated “D10.5”) was collected within the west basin and distal from the shore at 10.5m water depth, and core “Distal 13.5m” (abbreviated “D13.5”) was collected from the slope connecting the west basin to the north basin of Linnévatnet at 13.5m water depth (Figs. 3,4). Cores (6.6 cm in diameter) were collected from boats and retrieved using a Universal Percussion Corer, outfitted with a slide hammer that was raised and lowered by a line to drive the core tube into the sediment.

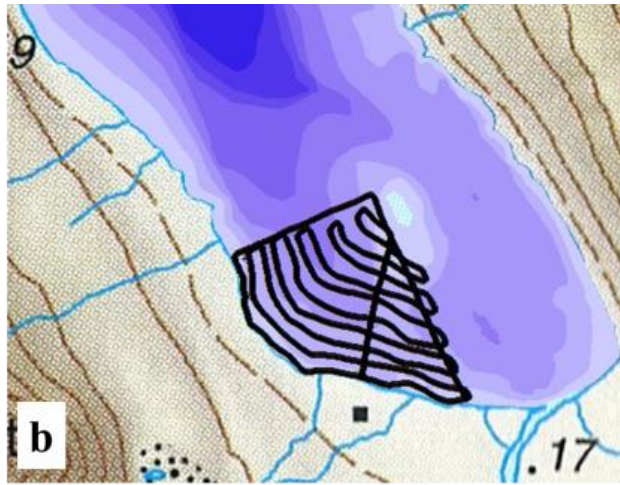
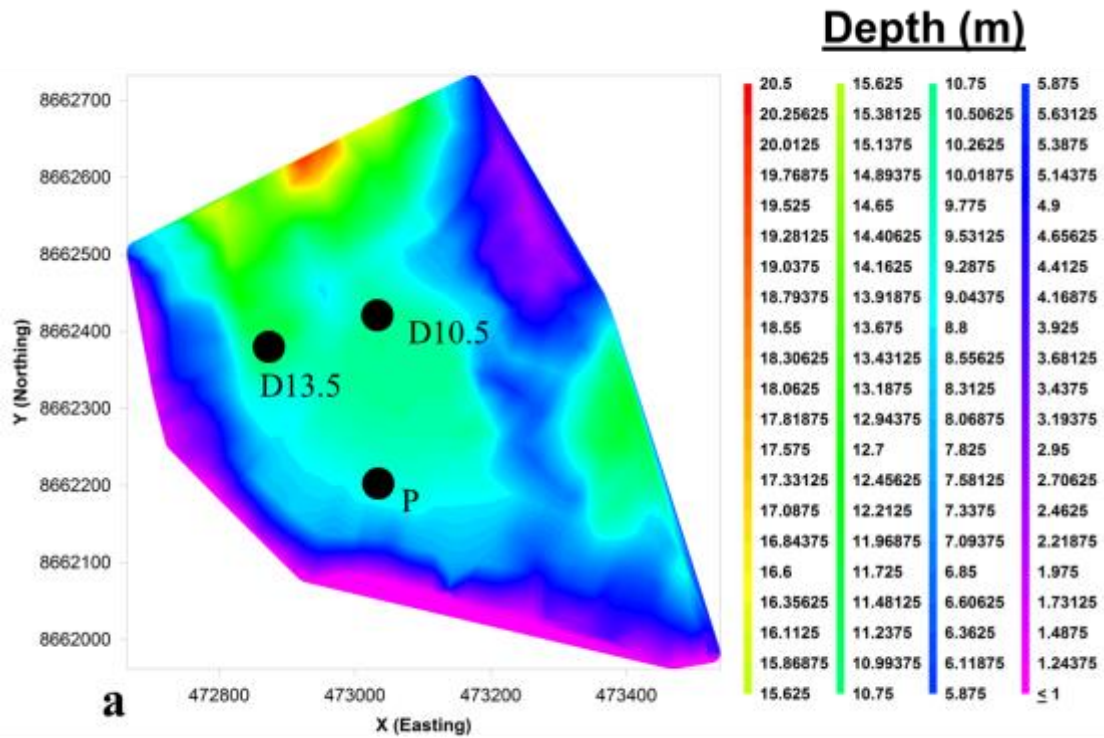


**Figure 3** (a) Bathymetric map of the Linnévatnet west basin, plotted in DPlot from bathymeter data, with location of core sites indicated. The contour scale indicates depth in meters. (b) Tracks over which bathymeter data was collected. Both images are adapted from maps plotted by Steven Roof, Hampshire College.

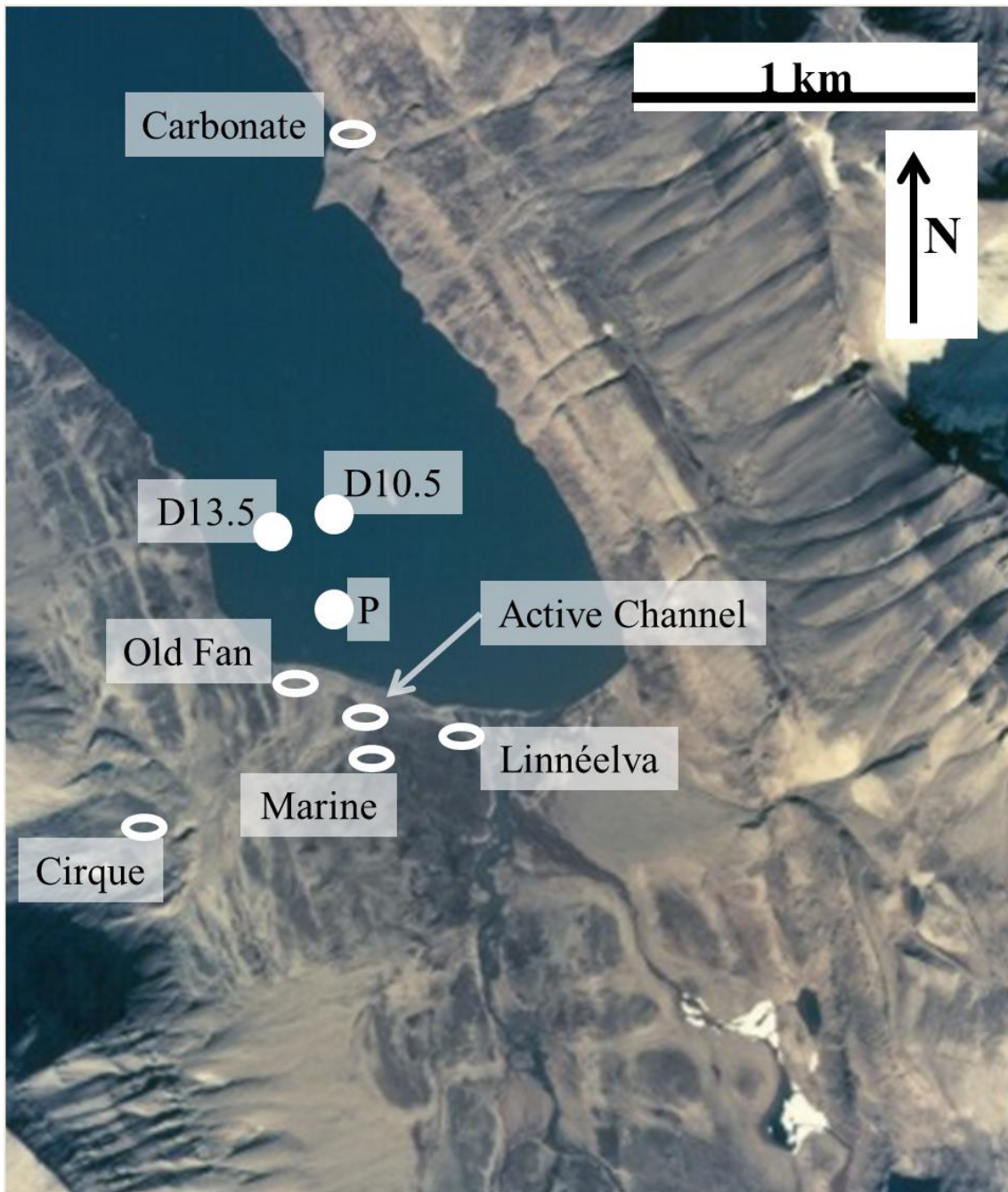


**Figure 4** Aerial photograph (1995; Norsk Polarinstitutt) of Linnévatnet's southern shore with sample site locations indicated. Lake sediment core sites are represented by white circles, while surficial sediment sample sites are represented by open ovals.

In addition to lacustrine sediment cores, fine-grained surficial sediment samples (silt-to-clay) were collected from six sites in Linnédalen (Fig. 4). Sediments were scraped from the surface of fine-grained deposits contained within evaporated pools or overbank

regions near actively flowing channels. The samples were chosen because they represent “end member” specimens of the various sediment sources to Linnévatnet. Cirque and cirque drainage (Old Fan and Active Channel) sediments, eastern-wall carbonate sediments (Carbonate), and the sediments carried by Linnéelva were identified as the dominant source sediments of the west basin by Snyder et al. (2000). A sample of the Linnédalen glacial marine sediment (Marine Mud) was also collected due to its presence across the valley floor and field observations of solifluction and slumps of this sediment along the shores of Linnévatnet.

All samples (cores and surficial sediments) were stored at external temperatures (~5°C) until 31 July, 2013, at which point they were transported from the field site until 5 August, 2013, and were thereafter stored at 4°C. Prior to transport, upper portions of core tubes were cut to <4cm above the sediment-water interface, and sodium polyacrylate (Brand: Zorbitrol) powder was added to absorb water and provide a firm substrate adjacent to the sediment (Tomkins et al., 2008).

### *Laboratory and Analytical Methods*

#### *Core and Sediment Preparation*

At the Quaternary Geology Laboratory of University of Massachusetts—Amherst, core tubes were split with an oscillating saw, and core halves were separated by running fishing line between the split portions of the core tubes. The exposed surface of each core half was cleaned and smoothed with a razor blade by wiping the surface parallel to visible laminations. Samples were later transported to Bowdoin College, where the visual stratigraphy of cleaned core-half surfaces was logged for each core.

To prepare surficial sediment samples for geochemical analyses, the interior of a 38-cm-long core tube half was divided into six sections using 2-cm-wide floral foam sections. The intervening space was then filled with one of the six surficial sediment samples, and the surface of each sediment segment was cleaned and smoothed with a razor blade (Fig. 5). Any observable debris was removed from sediment samples while transferring them to the core-half. This half “core” is henceforth referred to as the “artificial core.”

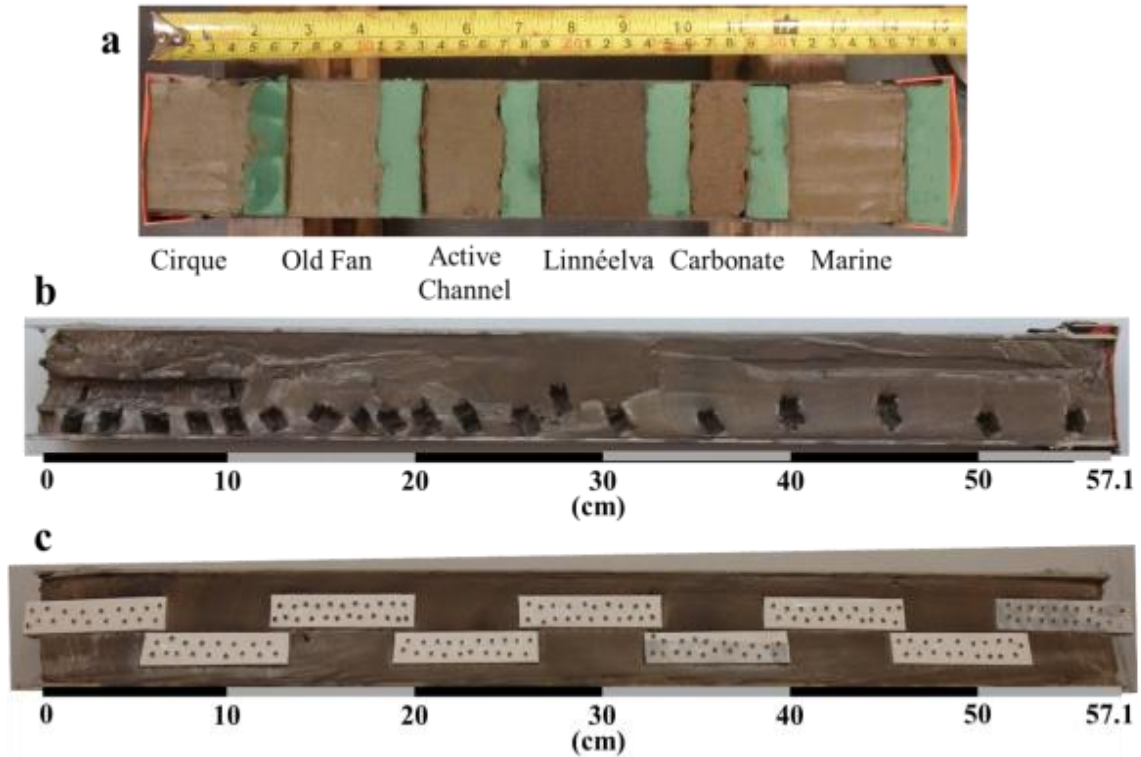


**Figure 5** Images of various core preparation and laboratory methods. (a) Artificial core with different sediment sources indicated. The green intervening regions are floral foam. Note that this image is not to scale with Figs. 5b and 5c. (b) Core D10.5 half used for chronostratigraphic subsampling. The region continuously sampled for  $^{239+240}\text{Pu}$ -based dating can be seen in the central upper 10cm, and variable interval sampling for chemostratigraphy can be seen down the entire core length. Stratigraphic up is oriented to the left. (c) Core D10.5 half used for thin-section subsampling. Note that the trays overlap adjacent trays or sediment edge by at least 1cm. Stratigraphic up is oriented to the left.

### Geochemistry and Physical Parameters

Profiles of colorimetric lightness ( $L^*$ ) and magnetic susceptibility ( $\kappa$ ) were collected at 5-mm intervals with a GeoTek Multisensor Core Logger at the University of Massachusetts—Amherst. All three lake sediment cores as well as the artificial core were analyzed, and prior to analyses, cleaned core-half surfaces were covered with a commercial plastic film. The spectrophotometer aperture is 8 mm in diameter, and the magnetic susceptibility sensor has an active sensing surface of a 10.5 mm x 3.8 mm rectangle contained within a 25-mm ceramic cylinder. For spectral reflectance measurements at each interval, GeoTek software calculated colorimetric parameters in *Lab* and CIE 1931 XYZ color spaces. All spectral and magnetic-susceptibility



measurements that overlapped with core caps or core-top sodium polyacrylate were not included.

XRF elemental profiles were measured for core D10.5 at 500- $\mu$ m intervals and for the sediment regions of the artificial core at 760- $\mu$ m intervals with an ITRAX Core Scanner at University of Massachusetts—Amherst. Prior to XRF scans, cleaned core/artificial core surfaces were covered with a mylar film. For all XRF analyses, a molybdenum tube was used and parameters were as follows: 10 s exposure time, 30 kV voltage, and 55 mA current. Peak areas (area beneath the XRF peak) were measured for the elements Al, Si, Ar, K, Ca, Ti, V, Cr, Mn, Fe, Ni, Cu, Zn, Ga, As, Rb, Sr, Y, Zr, Pd, Ba, La, Ce, Sm, Eu, Tb, Dy, Er, Hf, Ta, W, Re, Os, Ir, Pt, Au, Hg, Bi, and U.

### Chronostratigraphy

Two different chronostratigraphic techniques were applied to core D10.5 to constrain downcore ages.  $^{239+240}\text{Pu}$  radionuclide dating involves correlating core intervals exhibiting maxima in  $^{239+240}\text{Pu}$  concentration with periods of peak radionuclide fallout during 1963/1964 peak nuclear weapons testing and the 1986 Chernobyl accident (Ketterer et al., 2004). For  $^{239+240}\text{Pu}$ -based dating, the upper 10.8 cm of core D10.5 was subsampled at ~5mm intervals (20 samples total; Fig. 5). Care was taken to collect samples no greater than 1.5 cm across or 1cm deep into the sediment, and samples were collected down the center of the core to avoid sampling overlying sediments that were deformed by the coring process into an adjacent position. Samples were placed in an oven to dry at 100°C for several days. Following drying, samples were individually ground in a stainless-steel ball mill for 5 minutes. Ball mill cylinders and bearings were rinsed with deionized water between samples to ensure that there was no cross-contamination. Pulped samples were weighed and transferred to 20-ml glass scintillation vials, which were then shipped to Dr. Michael Ketterer's lab at the Metropolitan State University of Denver Department of Chemistry for analysis. A downcore  $^{239+240}\text{Pu}$  concentration curve was developed from Inductively-Coupled Plasma Mass Spectrometry (ICP-MS) analyses of the 20 subsamples using the methods outlined in Ketterer et al. (2004).

A chemostratigraphic method was used to estimate the 1850 CE horizon in core D10.5 by measuring increases in trace metal concentrations associated with elevated anthropogenic fossil fuel burning and atmospheric deposition of trace metals (ca. 1850 CE). Twenty subsamples measuring approximately 1.5 cm<sup>3</sup> (1-cm stratigraphic depth, 1 cm into core half, 1.5 cm parallel to laminations) were collected at variable intervals spanning the entire depth of core D10.5. Each subsample was collected along the side of the core, but laminations were followed from the core center to account for sediment deformation (Fig. 5). Because the 1850 horizon was expected to lie within the upper third of core D10.5, the upper 20 cm were sampled at 2-cm intervals, transitioning to 5-cm intervals in the lower core (Fig. 5). Subsamples were dried at 50°C for several days, and each was ground in a stainless-steel ball mill for 5 minutes. Ball mill cylinders and bearings were rinsed with deionized water between samples to prevent cross-contamination. Pulped samples were weighed, transferred to 20-ml glass scintillation vials, and shipped to Acme Labs, Inc, where aqua regia digestion and ICP-MS were performed for the elements Au, Ag, Al, As, B, Ba, Bi, Ca, Cd, Co, Cr, Cu, Fe, Ga, Hg, K, La, Mg, Mn, Mo, Na, Ni, P, Pb, S, Sb, Sc, Se, Sr, Te, Th, Ti, Tl, U, V, W, and Zn. ICP-MS concentration values were then normalized with Al, a conventional and effective lithogenic reference element, which can be used to distinguish non-natural (i.e. anthropogenic) enrichment of a given element in sediments (Boës et al., 2011).

### Thin-Sections

Preparation of thin-sections was modeled after the methods of (Dowey, 2013). Rectangular trays with an area of 7.4 cm x 1.7 cm and a depth of 0.9 cm were cut from aluminum sheeting and folded. Holes 2.3mm in diameter and <1cm apart were drilled into the trays to allow fluid to more readily diffuse into the trays. Nine trays in total were pressed into core D10.5, alternating left to right downcore and overlapping by at least 1cm with each adjacent tray (Fig. 5). Trays 1 and 9, occupying the top and bottom of the core, also extended approximately 1cm beyond the edge of the core (Fig. 5). After all trays were placed into the sediment so that their tops were flush with the sediment surface, each tray was removed by passing a metal spatula beneath it and lifting the sediment-laden tray out of the core sediment. The trays were wiped clean, except

wherever a rock extruded from the surface, and then placed in a single plastic, airtight container.

The sediment-laden trays were bathed in histological grade acetone in a sealed container. At 8- to 24-hour intervals, the acetone wash was removed by pipette, replaced with fresh histological grade acetone, and the container was resealed. Before disposal, the extracted acetone solution was placed in a graduated cylinder and the specific gravity was measured with a hydrometer to ensure that specific gravity of the solution was approaching the specific gravity of pure acetone (0.791). Eight exchanges of histological grade acetone were performed, after which histological grade acetone was replaced by EM grade acetone for two 24-hour washes. Subsequent baths contained some fraction of Spurr Low Viscosity Embedding Media (epoxy): containing ERL 4221 (7-Oxabicyclo [4.1.0] heptane-3-carboxylic acid, 7-oxabicyclo [4.1.0] hept-3-ylmethyl ester), diglycidyl ether of polypropylene glycol, nonenyl succinic anhydride, and dimethylaminoethanol at a mass ratio of 106.7:37.1:153.51:2.6, respectively. Following the ten acetone baths, the sediments were bathed in a 50% epoxy-50% acetone (volumetric) mixture and then a 65% epoxy-35% acetone (volumetric) mixture, each for 24 hours. After the second acetone-epoxy mixture was removed, the sediments were bathed in undiluted epoxy and cured uncovered at 50°C for 72 hours, at which point the epoxy could not be scratched or depressed by a fingernail. The hardened epoxy block was then removed from the container, each sediment segment was cut from the block and trimmed with a rock saw, and the segments were sent to Quality Thin Sections in Tuscon, Arizona, to be prepared into oriented thin sections. Following preparation of thin-sections, reflective digital scans of thin-sections were collected with an EPSON 4490 Photo Scanner, and thin-section images were aligned in Adobe Photoshop to create a thin-section reconstruction of core D10.5. Thin-sections were searched microscopically for the presence of coupled laminae or varve<sup>1</sup> structures, and depth ranges characterized by abundant and well-defined, light-colored laminae were recorded.

---

<sup>1</sup> First described by Gerard De Geer in 1912, varves are annual sedimentation layers comprised of lamination couplets. In Lake Boldterskardet, Svalbard, a characteristic varve is comprised of a silt layer, deposited during the hydrologically active spring and summer, which grades up into a fine clay layer, deposited during calm periods of ice-cover in the autumn and winter (Guoqiang et al., 2006).



## Results

### *Chronostratigraphy*

A single peak in  $^{239+240}\text{Pu}$  activity (with standard deviation) of  $5.05 \pm 0.24$  Bq/kg occurs at a depth of 1.89 cm (vertical center of ~0.54-cm-deep subsample), with activity of  $1.48 \pm 0.11$  Bq/kg in the underlying subsample (2.43 cm depth) and an activity of  $0.68 \pm 0.12$  Bq/kg in the overlying subsample (1.35 cm; Fig. 6). For all other subsamples from core D10.5,  $^{239+240}\text{Pu}$  activity measurements were below the detection limit of 0.5 Bq/kg (Fig. 6; Ketterer, pers. comm., 2014).

Among the geochemical profiles measured with ICP-MS, profiles of Al-normalized Ba, Cr, Hg, and Na exhibit sustained increases above maximum downcore values in the uppermost portions of the core (Fig. 7). Rises in aluminum-normalized Hg and Na concentration above peak downcore values occur at 10cm (Fig. 7). Hg decreases below maximum downcore values at 6 cm depth, but this decrease is well within the range of the wide fluctuations observed in the upper 20 cm of core D10.5 (Fig. 7). In addition, there are accelerated increases in Hg and Na as well as rises in Ba and Cr above downcore values from 4 cm to the core top (0 cm; Fig. 7). The precise value for Cr/Al at 4cm depth (30.05) is actually slightly less than the value at 18cm (30.54), but Cr/Al increases rapidly between 4cm and 2cm depth to 40.58 (Fig. 7). The maximum downcore Ba/Al value preceding 4cm depth is a distinct, isolated peak at 350cm depth (Fig. 7).

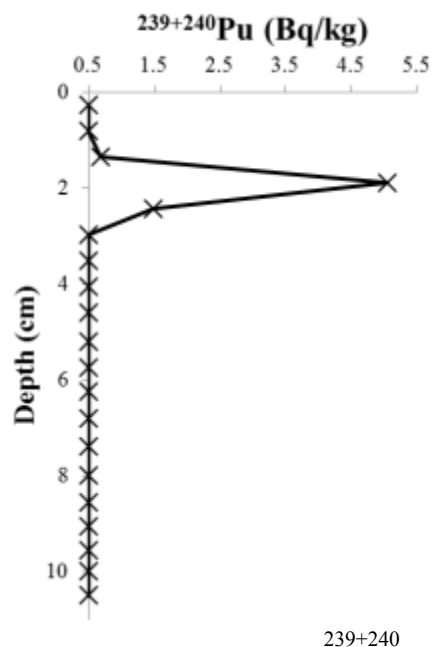


**Figure 6** Profile of  $^{239+240}\text{Pu}$  radionuclide activity for core D10.5, measured at ~5mm intervals. All measurements below the detection limit (0.5 Bq/kg) are plotted at 0.5 Bq/kg. Peak activity of 5.05 Bq/kg occurs at 1.89m depth.

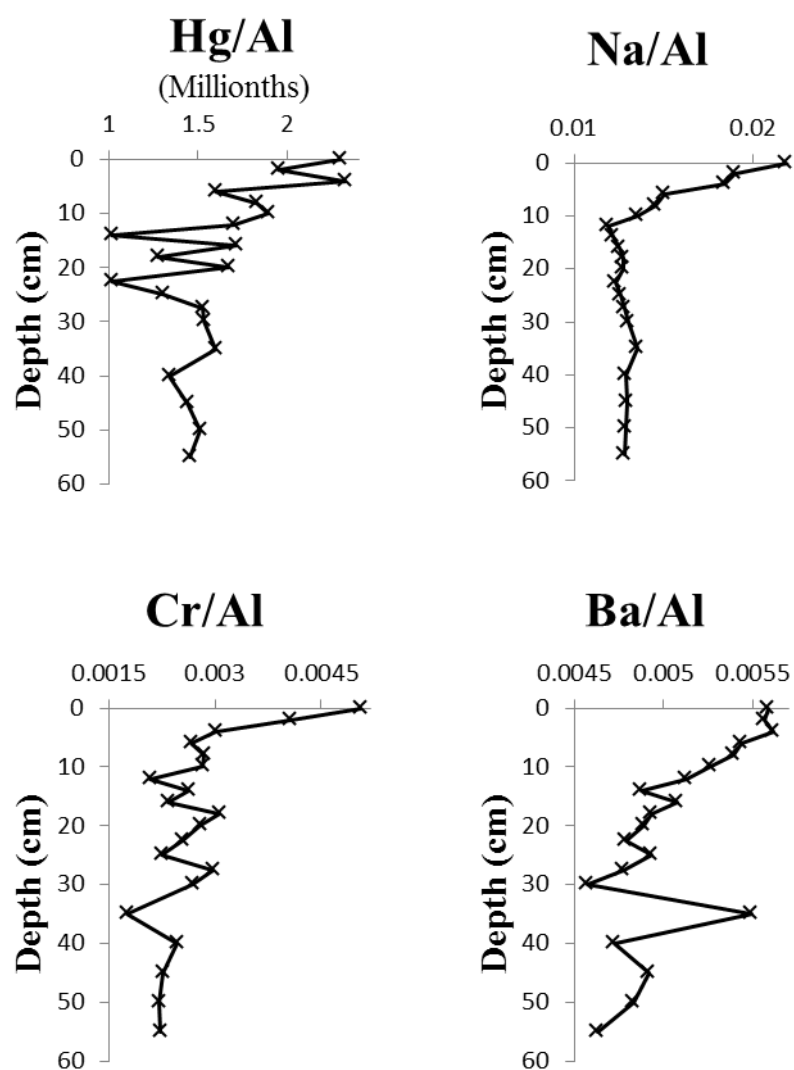


**Figure 7** Al-normalized profiles of Hg, Na, Cr, and Ba for core D10.5, measured with ICP-MS. Concentrations for the various elements were measured in mass percent, and the Hg/Al plot is presented in millionths. Hg/Al and Na/Al rise above background levels at 10 cm depth. Cr/Al and Ba/Al increase above background levels at 4 cm depth.

### *Visual Stratigraphy*

The length of core D10.5 is characterized by massive, fine-grained, cohesive brown-gray sediment, with local light-colored laminae (Fig. 8). The sediment is predominantly fine-silt to clay, although some light-colored laminae comprise coarser silt (grain sizes estimated). Deformation of core sediment during coring is observed from the curvature of distinct laminae, indicating asymmetric deformation that is most pronounced between 13 cm and 35 cm depth. Based on visual observation of the split-core surface, there are two regions of abundant light-colored (yellowish to cream-colored) laminae (2-12.5 cm and 42.2-46.4 cm depth), a region with a yellow hue to the massive brown-gray sediment (28-31.7 cm depth), and three distinct laminae of different colors: an isolated yellow lamina at 32.8 cm depth, a thicker dark brown lamina spanning 34.6-35.3 cm, and a pink lamina spanning 39.1-39.3 cm depth (Fig. 8).

Thin-sections allow microscopic analysis of stratigraphy. The sediments of the fourth and sixth slides (from the stratigraphic top of the core) were damaged during production, but the margins can be analyzed to sufficiently identify sediment color (Fig. 8). Additionally, a portion of the record in the third slide from the core top is lost, but based upon visual observation of the core-half surface this region exhibits no evidence of lamination (Fig. 8). The only laminae continuous between adjacent slides were observed in the slide pairs 1-2 and 7-8 (Fig. 8). No coupled laminae or varve-like structures could be discerned in macroscopic or microscopic observations of core D10.5. Regions of abundant and well-defined, light-colored laminae were observed in the following depth ranges: 0-12.3 cm, 29.5-31.8 cm, 41.2-47.8 cm (Fig. 8). Using an age-depth model extrapolated from sedimentation rates (see Discussion), these regions of abundant light-colored laminae correspond with the date ranges 984-1082 CE, 1329-1363 CE, and 1816 CE-Present (Fig. 9, 10). Microscopic analysis also revealed the presence of millimeter to sub-millimeter scale orange mottling superimposed upon the sediment texture, observed in the depth ranges 25.0-28.2 cm, 42.5-44.5 cm, and 48.4-49.5 cm (Fig. 8). Such orange mottling was only observed at ~44.5 cm depth on the freshly split-core surface, but the mottling has increased during storage, suggesting that it represents post-collection redox reactions.

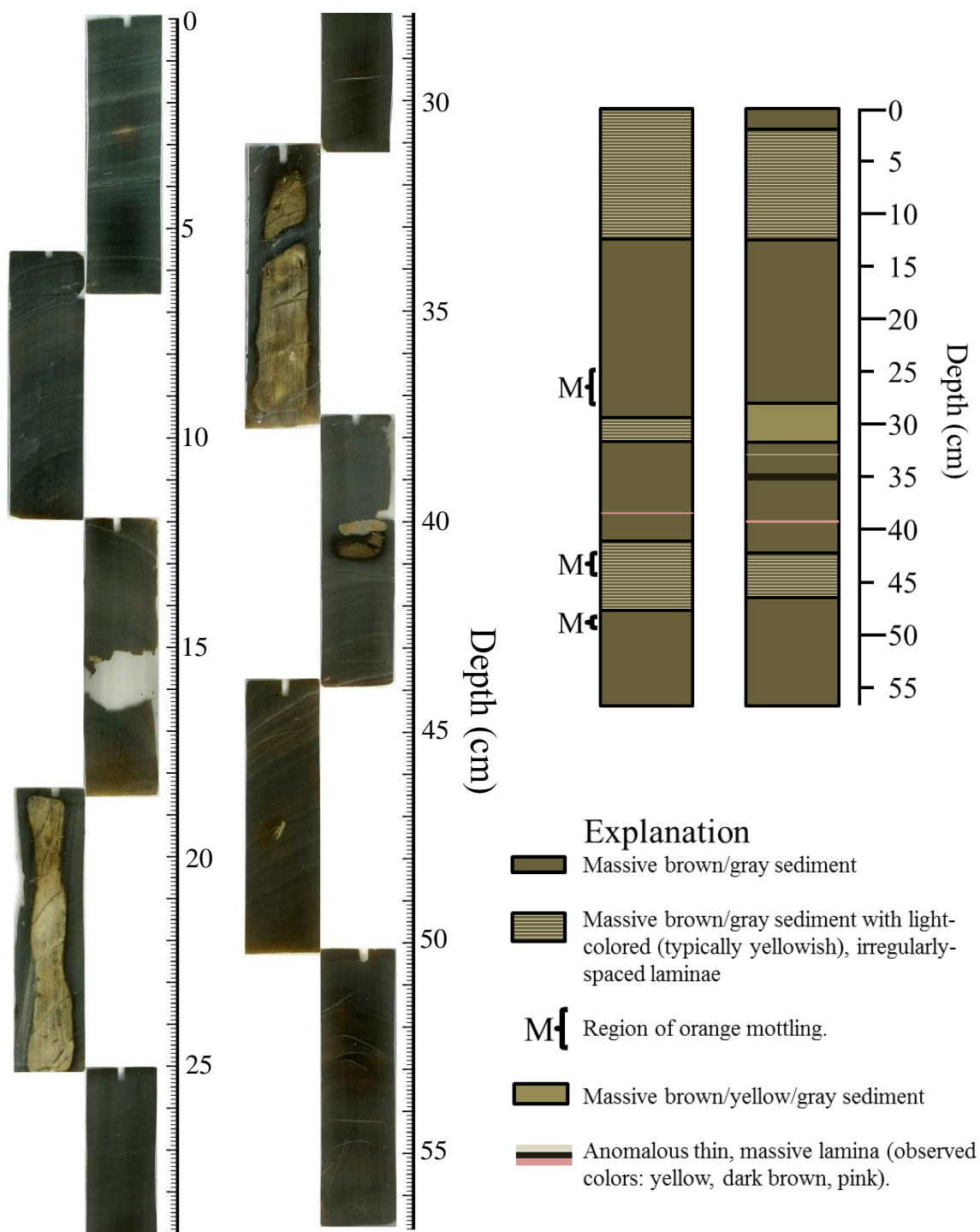


**Figure 8** Reconstruction of core D10.5 from aligned, thin-sections (digital scans with enhanced contrast) and stratigraphic logs of core D10.5 derived from microscopic analysis of thin-sections (I) and visual observations of the split-core surface (II). Pink layers in I and II are identical and the individual yellow laminae in II corresponds with the base of the middle laminated region in I. The dark layer observed in II was not observed in thin-section. Orange mottling observed in I is superimposed upon the texture of the sediment.

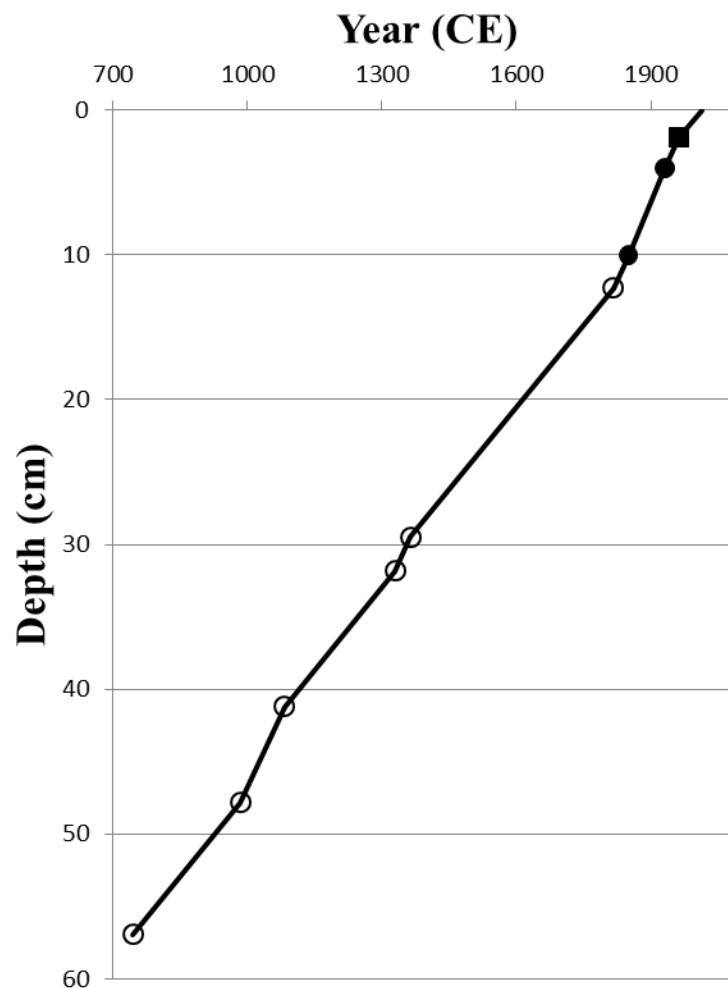


**Figure 9** Age-depth model for core D10.5 derived from  $^{239+240}\text{Pu}$  radionuclide dating (1963/4 CE; ■), chemostratigraphic dating (1932 and 1850; ●), and extrapolated sedimentation rates. A sedimentation rate of  $0.38 \text{ mm yr}^{-1}$  is applied to non-laminated depth ranges, while a rate of  $0.67 \text{ mm yr}^{-1}$  is applied to laminae-rich ranges. The boundaries between laminae-rich and non-laminated depth ranges are indicated by ○. The top of core D10.5 is assumed to represent the date of core collection (2013 CE).

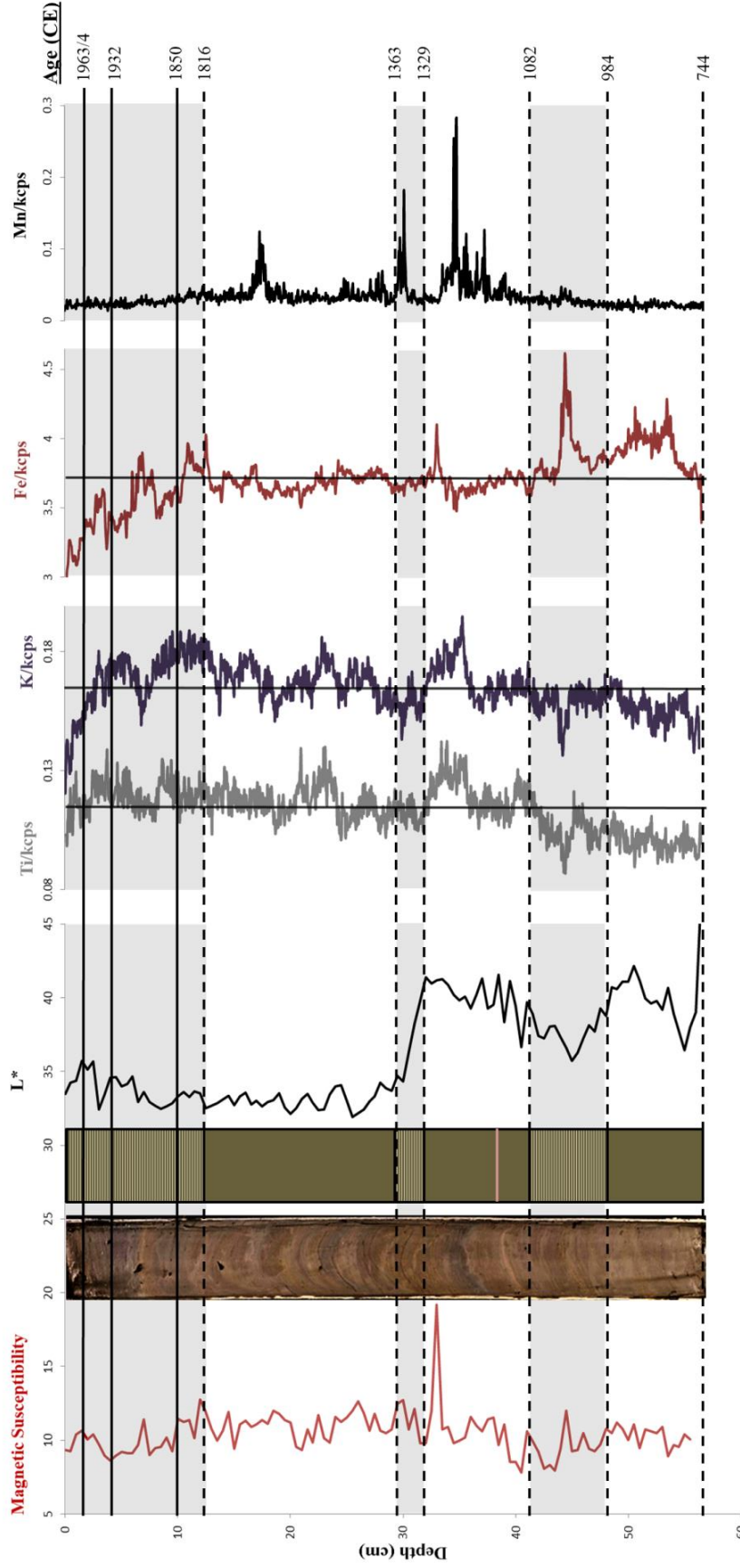


**Figure 10** Geochemical and physical parameter profiles of core D10.5. The dimensionless parameters magnetic susceptibility ( $\kappa$ ) and colorimetric lightness ( $L^*$ ) are measured at 5mm intervals. XRF profiles of Ti, K, Fe, and Mn are measured at 500 $\mu$ m intervals, and values represent peak area normalized by kilocounts per spectrum (kcps). Vertical lines superimposed on profiles of Ti, K, and Fe represent whole-core means. Shaded areas represent portions of core with abundant light-colored laminae. An enhanced-contrast image and thin-section-based stratigraphic log (see Fig. 8) of core D10.5 are shown for reference. Solid black lines represent absolute ages based upon  $^{239+240}\text{Pu}$  radionuclide dating (1963/64) and chemostratigraphic dating (1932, 1850 CE), while dashed lines represent ages calculated from sedimentation rates (see Fig. 9).

Comparison between stratigraphic logs derived from the split-core surface and thin-sections show that there is likely some error in the alignment of the thin-sections, as the yellow lamina observed at 32.8 cm depth in the split-core surface appears to correspond to the base of the middle laminated portion at 31.8 cm in the thin-section reconstruction (Fig. 8). Similarly, the distinct pink lamina observed at 39.2 cm depth on the split-core surface is observed at 38.3 cm in the thin-section reconstruction (Fig. 8).

### *Geochemistry and Physical Parameters*

#### *Source Sediments*

Cirque, Old Fan, Active Channel, and Linnéelva sediment samples exhibit clay to silt texture, while the Marine Mud sediment sample is a fine, cohesive clay with occasional shell fragments. The Carbonate sediment sample is approximately sandy in texture and includes shell fragments, likely derived from local marine sediment that had been reworked and incorporated into the sediment.

Table 1 contains relevant values of XRF, magnetic susceptibility ( $\kappa$ ), and colorimetric lightness ( $L^*$ ) for the six end-member source sediments of Linnédalen. Ti/kcps is substantially higher in sediments associated with the west basin cirque and its drainage (Cirque, Active Channel, Old Fan), even when taking into account standard deviation ranges (Table 1). K/kcps and Fe/kcps are similarly higher for cirque-associated sediments and Marine Mud, although Fe/kcps is higher for Marine Mud than cirque-associated sediments (Table 1). Mn/kcps is greatest in Marine Mud, next highest in Old Fan sediment, and comparable among the Linnéelva, Cirque, and Active Channel sediments (Table 1). Carbonate sediment consistently exhibits the lowest XRF signals of the various source sediments (Table 1). Marine Mud exhibits a magnetic susceptibility nearly twice as great as the other sediments, and Old Fan sediments have a magnetic susceptibility slightly elevated relative to sediments other than Marine Mud (Table 1). Lightness is highest in Carbonate sediment and lowest in Linnéelva sediment, although standard deviation ranges overlap among the six source sediments (Table 1).

	<b>Ti</b>	<b>K</b>	<b>Fe</b>	<b>Mn</b>	<b>κ</b>	<b>L*</b>
<b>Cirque</b>	12.4 ± 0.8	14.0 ± 1.9	336 ± 6	1.88 ± 0.35	10.00 ± 0.29	36.60 ± 0.34
<b>Old Fan</b>	12.7 ± 0.6	13.3 ± 2.7	346 ± 5	2.19 ± 0.31	12.59 ± 1.09	35.90 ± 1.33
<b>Active Channel</b>	12.2 ± 0.9	12.8 ± 0.8	322 ± 5	1.81 ± 0.30	10.65 ± 0.93	37.05 ± 1.19
<b>Marine Mud</b>	9.8 ± 0.5	12.1 ± 2.1	358 ± 4	2.51 ± 0.39	20.9 ± 1.78	36.73 ± 2.02
<b>Linnéelva</b>	9.1 ± 1.2	7.8 ± 1.6	214 ± 10	1.84 ± 0.56	10.42 ± 0.65	34.73 ± 1.94
<b>Carbonate</b>	4.8 ± 0.9	5.2 ± 0.9	158 ± 12	1.52 ± 0.33	10.6 ± 1.91	38.67 ± 3.11

**Table 1** Mean geochemical signatures of the various “endmember” source sediments in the Linnédalen system. XRF signatures of Ti, K, Fe, and Mn are measured in peak area, normalized by kilocounts per spectrum (kcps), and values are presented multiplied by 100. Magnetic susceptibility (κ) and the colorimetric parameter lightness (L\*) are presented as measured. Means of all values are presented with ± one standard deviation. Note that Cirque, Old Fan, and Active Channel represent sediments associated with the west basin cirque and its drainage.

### Geochemical and Physical Profiles of Core D10.5

The majority of XRF elemental profiles for core D10.5 exhibit low signal-to-noise ratios, except profiles for the elements Ti, K, Fe, and Mn (Figs. 10, 11). Comparison between XRF and ICP-MS data for these elements show that there is good agreement between the two analyses for broad trends in Fe and Mn, while there is poor agreement between the XRF and ICP-MS profiles of Ti and K (Fig. 11, See Appendix). XRF profiles of Ti/kcps and K/kcps are more-or-less in-phase (Fig. 10). Exceptions to this tendency are a local K/kcps minimum at 13.65 cm depth with no comparable change in Ti/kcps, as well as three instances where changes in K lag those of Ti: minima of K/kcps occur 0.1 cm and 1.9 cm upcore of Ti/kcps minima at 44.05 cm and 8.65 cm depth, respectively, and a steep upcore increase in Ti/kcps at 35.4 cm is followed by a similar increase in K/kcps at 35.0 cm (Fig. 10). Additionally, K/kcps decreases considerably upcore beginning at approximately 3 cm depth, while Ti/kcps decreases less so and with wider variation about the trend (Fig. 10). XRF profiles of Ti, K, Fe, and Mn do not exhibit sustained changes through abundantly laminated sections of core D10.5 (Fig. 10). However, Ti/kcps exhibits a sustained increase above the lowermost laminated range, such that the average value of Ti/kcps downcore of the lowermost laminated zone is 0.10, while the average value above this range is 0.12 (Fig. 10). Furthermore, the two upper laminated sections are associated with gradual increases interrupted by abrupt decreases



in Ti/kcps, while the correlative changes in K/kcps are relatively more gradual (Fig. 10). There is also a decreasing trend in Fe/kcps beginning at the base of the uppermost laminated zone and continuing to the core top (Figs. 10, 11). Otherwise, Fe/kcps is characterized by an increase from the core bottom to ~53 cm depth, a gradual upcore decrease from ~53 cm to ~34 cm depth, and distinct peaks at 32.85 cm and 44.15 cm depth (Figs. 10, 11). Fe/kcps varies subtly but similarly to Ti/kcps and K/kcps between 32 cm and 12.3 cm (Figs. 10, 11). Mn/kcps remains fairly constant but is punctuated by peaks at 30 cm and 17.4 cm, and a range of elevated Mn signal between 37.5 cm and 33.4 cm with an especially large peak at ~34 cm (Figs. 10, 11).

Magnetic susceptibility varies subtly across core D10.5 and is characterized by a pronounced peak at 33 cm depth and a decreasing upcore trend across the uppermost abundant laminae range (Fig. 10). Lightness decreases across the middle abundant laminae range from values consistently above 35 (and typically as high as 40) to values consistently below 35, although there is a subtle increasing trend in  $L^*$  starting at 6 cm depth and proceeding upcore (Fig. 10).

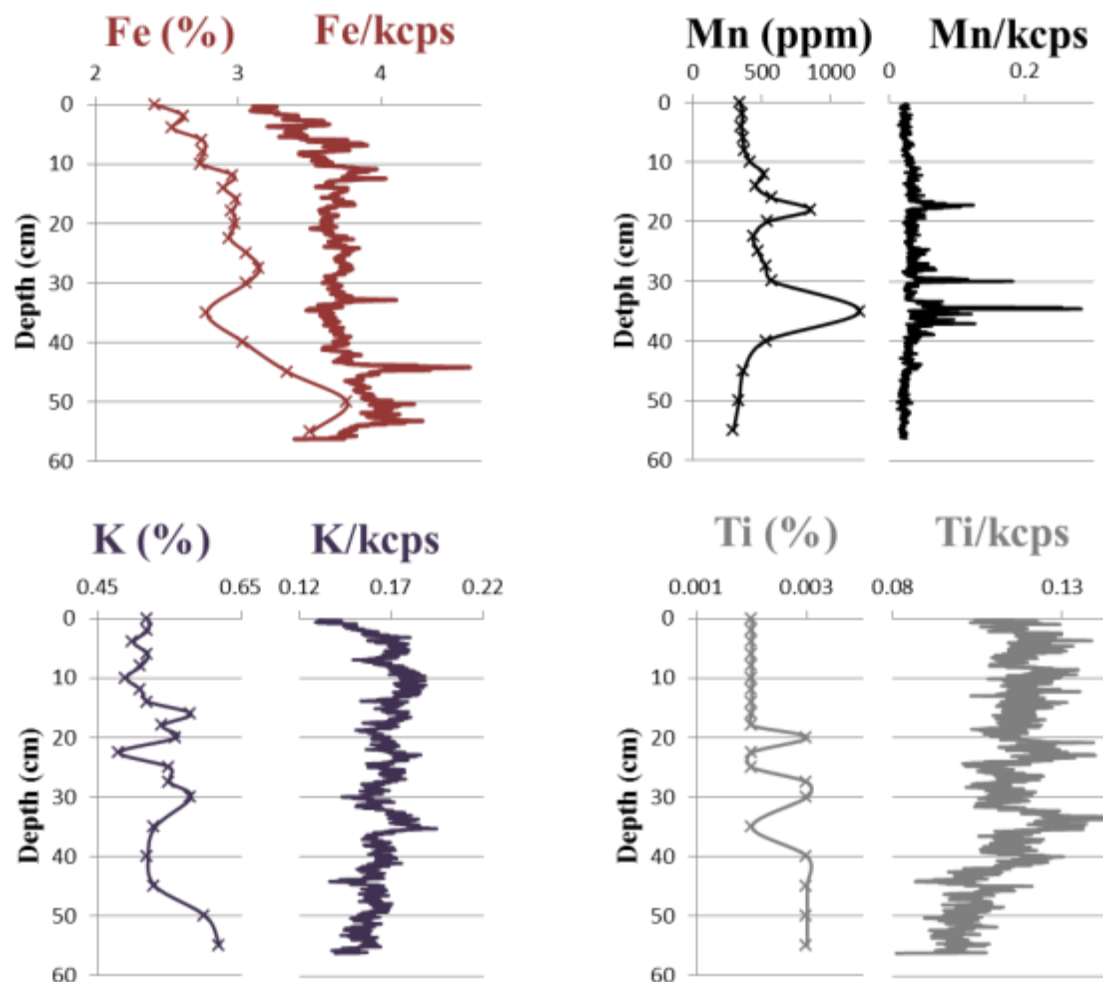


**Figure 11** Comparison of XRF data (continuous curves) and ICP-MS data (x's) from core D10.5, plotted as a function of depth, for the elements Fe, Mn, K, and Ti. ICP-MS data are measured as proportions of sample mass, while XRF data is measured in peak area and normalized by kilocounts per spectrum (kcps). Large scale patterns are in agreement between XRF and ICP-MS data for Fe and Mn, but not between XRF and ICP-MS data for K and Ti.

## Discussion

### *Chronostratigraphy*

Chronostratigraphic techniques provide a chronology for the upper 10cm of core D10.5.  $^{239+240}\text{Pu}$  activity in lacustrine sediment typically exhibits two maxima (1963/64 peak testing and 1986 Chernobyl fallout), but given the low sedimentation rate, the 1986 peak would fall within the subsequent upcore interval (1.35 cm), which is nonetheless elevated above background levels (Fig. 6). Ultimately, the measured peak  $^{239+240}\text{Pu}$

activity in the interval centered at 1.89 cm depth is sufficient for a confident interpretation as the 1963/64 fallout horizon (Ketterer, pers. comm., 2014).

Increases in Al-normalized Hg and Na above background levels at 10 cm likely reflect the increased atmospheric transport and deposition of Hg and Na from anthropogenic emissions beginning ca. 1850 CE. Hg accumulation rates in several Svalbard lakes have increased significantly above background levels since ca. 1850 CE (Drevnick et al., 2012). Although Hg falls back below background levels at 6 cm depth, it increases to its greatest value in core D10.5 in the subsequent upcore interval (4 cm depth). Furthermore, Hg fluctuates considerably between adjacent subsample intervals, and the decrease in Hg at 6 cm depth is well within the range of these fluctuations. Therefore the observed increase of Hg above background levels at 10 cm depth is interpreted as a minimum depth and the best estimate for the 1850 CE horizon. In addition to Hg, evidence supports long-distance atmospheric dispersion and deposition of particulate Na from anthropogenic sources, which include coal combustion, metallurgical processes, and refuse incineration (Harrison et al., 1997; Ooki et al., 2002). However, the increase in Na at 10 cm depth must be interpreted with some caution as an indicator of atmospheric deposition. Zorbitrol (sodium polyacrylate) was used to gelify the water-sediment interface in the core tube prior to shipment, and there may have been Na transfer across the interface that contaminated the uppermost portion of core D10.5. The gradually decreasing Na concentration downcore from 0-10 cm is consistent with potential Na enrichment from the Zorbitrol powder, which was introduced at the core surface. No information on the tendency of dissociated Na from sodium polyacrylate to penetrate sediment could be found, but sodium polyacrylate treatment of sediment-water interfaces does not affect sediment carbon or nitrogen levels (Tomkins et al., 2008). Furthermore, the fine-grained nature of the sediment and its relative cohesiveness seems to suggest that any Na contamination would be minimal. Nonetheless, increases in Na within the upper 10 cm of core D10.5 are interpreted only tentatively as the result of atmospheric deposition of anthropogenic Na.

Accelerated upcore increases in Hg and Na as well as rises in Ba and Cr from 4 cm depth to the core top are interpreted as robust indicators of increased atmospheric deposition of metal pollutants from nearby anthropogenic sources, including

Longyearbyen (established 1906 CE; 47 km away) and Barentsburg (established 1932 CE; 10 km away). The abrupt increases in Hg and Na suggest drastically increased deposition of these materials, consistent with a nearby rather than long-range source. Cr is commonly deposited from the atmosphere in close proximity to air pollution sources (Steinnes and Friedland, 2006). Berg and Steinnes (1997) found Cr accumulating in quantities above background levels within ~50 km of a ferro-chrome smelter, a prolific Cr source. Although Cr does not actually exceed background levels at 4 cm depth, the value is near enough to maximum background levels and the increase from 4 cm to 2 cm is so dramatic that 4cm is considered approximately the depth of increase above background levels. Ba is likely a good indicator of local coal burning since it is found in significant amounts in Svalbard coal (Orheim et al., 2007; Steinnes and Friedland, 2006). It is important, though, to consider whether the Ba observed in the Al-normalized profile does indeed represent atmospheric deposition of anthropogenic particulates or whether it represents sedimentary coal from Linnébreen and Linnéelva. The non-normalized Ba profile of core D10.5 exhibits a noisy profile without a clear trend, indicating no net increase in Ba delivery to Linnévatnet, while the increase in Al-normalized Ba above the downcore maximum between 6 cm and 4 cm suggests a non-natural (i.e. anthropogenic) enrichment (See Appendix; Fig. 7; Boës et al., 2011). However, the net increase in Ba/Al from 30 cm to 4 cm suggests that there may be a pre-anthropogenic, but still likely geogenic, signal, and the nature of this needs to be more carefully investigated. Nonetheless, given the increases in all four trace metals near 4 cm depth, this horizon is interpreted as the best estimate for the onset of local coal burning.

The establishment date of Barentsburg (1932 CE) is chosen for the age of the trace metal increases at 4 cm depth because Barentsburg is substantially closer to the field site than Longyearbyen. The increases may represent elevated atmospheric deposition occurring as early as 1906 CE (Longyearbyen establishment), but given the limited range of atmospheric Cr transport from pollution sources and the relatively high mass of Ba, it seems unlikely that these materials would be transported in measurable quantities from as far away as Longyearbyen. Lastly, it is important to note that all interpretations of the core D10.5 chemostratigraphy rest upon the assumption that there was no change in the nature of sedimentation to the Linnévatnet west basin unaccounted for by Al-

normalization, and indeed there is no evidence of such change observed from the visual stratigraphies.

### *Sedimentation Rates & Age-depth Model*

Chronostratigraphic results provide sedimentation rates, which can be extrapolated to approximate a chronology for core regions below 10cm depth. Assuming the core top represents the modern surface (2013 CE), a reasonable assumption given the relatively undisturbed sediment-water interface of core D10.5, the 1.89 cm depth of the 1963/64  $^{239+240}\text{Pu}$  activity peak indicates a slow sedimentation rate of  $0.38 \text{ mm yr}^{-1}$  during this interval. In contrast, the calculated sedimentation rate within the 1932-1963/64 CE interval is  $0.67 \text{ mm yr}^{-1}$ . The sedimentation rate for the ca. 1850-1932 CE interval ( $0.73 \text{ mm yr}^{-1}$ ) is similar. Alternately, if 1906 CE is used as the date for the local burning effects, the sedimentation rate in 1906-1963/64 CE interval is  $0.37 \text{ mm yr}^{-1}$ , although as mentioned this date and the associated rate are likely not accurate interpretations.

The discrepancy in west basin sedimentation rates before and after 1963/64 CE is most readily explained by changes in sediment delivery resulting from changing glacial and/or meltwater erosion of the west basin cirque and cirque drainage. The 1963/64 CE-Present interval overlaps a region, which although laminae-rich, is associated with a deglaciated west basin cirque (Snyder et al., 2000). Furthermore, the sedimentation rate for this interval ( $0.38 \text{ mm yr}^{-1}$ ) is consistent with the rate determined by Snyder et al. (1994) for the west basin ( $0.36 \text{ mm yr}^{-1}$ ) during pre-LIA nonglacial periods of the Holocene. In comparison, the 1932-1963/64 CE interval overlaps a depth range characterized by abundant light-colored laminae (a proxy for glacial sedimentation; see below), and topographic maps from the 1930s indicate the presence of a glacier within the west basin cirque (Snyder et al., 2000). Therefore, this interval almost certainly represents an interval of active glacial erosion and meltwater sediment transport. From the sedimentation rates and stratigraphic evidence of glacial activity within the respective depth ranges, I extrapolated the age-depth model below the 1850 CE horizon. I follow the assumption that intervals of increased light-colored laminae abundance evidence periods of elevated sedimentation and therefore were characterized by the higher sedimentation rate of the 1932-1963/64 CE interval, while unlaminated regions were characterized by

the lower, non-glacial sedimentation rate (Figs. 9, 10). The 1932-1963/64 CE interval is chosen over the 1850-1932 CE interval because the 1932 CE age is better supported by chemostratigraphic data and a more precise date than ca. 1850 CE. The application of a higher sedimentation rate to laminated core sections is supported by the findings of elevated sedimentation rates in the laminated portion of a west basin core (Snyder et al., 1994). Additionally, evidence of differential sedimentation rates for glaciated and deglaciated conditions in the west basin cirque further motivates the rejection of the 1906 CE age at 4cm depth, which would imply approximately constant sedimentation rate (Snyder et al., 2000).

It is important to stress that the age-depth model presented here be considered an approximation for several reasons. Firstly, there are no direct chronological constraints for core D10.5 below 10 cm, merely the extrapolated sedimentation rates, and downcore sedimentation rates likely vary beyond the two calculated rates. Secondly, the depth ranges, to which the sedimentation rates are differentially applied, are derived from stratigraphic analysis of the thin-section reconstructed core D10.5, which exhibits ~1cm shallower depths relative to visual stratigraphic analysis in lower portions of the core (Fig. 8). The results of this alignment error must be considered, but this error is suspected to be within the potential variations in sedimentation rates in core D10.5 as well as the variation in sedimentation rates that results from alternate interpretations of chemostratigraphic data. Such variations in downcore sedimentation rates could be characterized, and the error mitigated, by establishing absolute age constraints (ex. radiocarbon) on deeper portions of core D10.5. Finally, the pink lamina observed in core D10.5, with the present age-depth model, is ascribed an age of 1160 CE, while two pink laminae observed in an 84cm core from the Linnévatnet north basin and age-constrained using an extrapolation of the varve record of Dowey (2013) are dated to 630-636 CE and ca. 1340 CE (Richter, pers. comm., 2014). This 180yr discrepancy between the younger lamina and the pink lamina in core D10.5 additionally suggests error in the age-depth model applied to core D10.5. However, it is important to use caution when correlating patterns between cores from the different basins, as the separate basins of Linnévatnet have been found to demonstrate unique stratigraphic characteristics (Snyder et al., 1994). Apparently similar laminae may not in fact be identical due to differences in

sedimentation and sediment sources of the two basins of Linnévatnet. Additionally, both of these dates lie beyond the varve-counted record of Dowey (2013), are similarly extrapolated from sedimentation rates, and therefore may also exhibit some error. Nonetheless, there is evidence for uncertainty in the age-depth model presented here, and therefore, the provided dates should be treated primarily as estimates. Precise absolute dating techniques are required to improve the estimates of this age model, and careful comparison of D10.5 stratigraphy to the stratigraphy of west basin cores with radiocarbon-constrained horizons, such as those studied by Snyder et al. (1994) and Snyder et al. (2000), offers potential for such age model improvements.

### *Visual Stratigraphy*

The laminated, silt-clay texture of the sediments of core D10.5 is consistent with observations of previous studies examining the upper lacustrine sequences of Linnévatnet (e.g. Svendsen and Mangerud, 1997). The pink lamina in core D10.5 offers little insight into cirque glacier activity of the western valley wall, as it is likely derived from the red sandstones of the Petrellskaret Fm on the eastern valley wall (Ohta et al., 1992; Svendsen and Mangerud, 1997). The regions of orange mottling observed in core D10.5, given their lack of textural variation from surrounding sediments and increasing appearance over time, are interpreted as regions of oxidized Fe, which occurred after core collection. Fe oxidation in sediment cores following collection, opening, and exposure to the atmosphere is a common occurrence (König et al., 2000), and for that reason the mottling is ignored in stratigraphic interpretations.

Comparison between the reconstructed thin-section record and the split-core visual stratigraphy shows that corresponding laminae (the pink lamina and the lowermost lamina of the middle laminated portion) are found at approximately 1cm shallower in the reconstructed thin-section core, relative to measurements of the split-core surface. This error is due to the inaccuracy involved in aligning the multiple thin-section pairs that lack distinct, corresponding laminae. The depths recorded for the split-core surface are considered to be most accurate, given that they were observed directly from the core and because of the likelihood for error in aligning thin-sections that lack sufficient correlatable laminae. However, given that observations of laminae on a microscopic scale

are more precise, the observations of the reconstructed core are used for stratigraphic analysis and age-depth model reconstruction. I assume that none of the record was lost from the core top or bottom during thin-section preparation due to space provided during the subsampling process. Therefore, the depths 0 cm and 56.7 cm are constrained, as well as the transitions between thin-sections 1 and 2 and between 7 and 8. With these constraints, thin-sections had to be aligned nearly end-to-end in order to fill the 56.7 cm of the core reconstruction, suggesting that ~2 cm was lost in unknown proportions from the upper and lower portions of each thin-section (except for the core top and bottom thin-sections). Error in the alignment of thin-sections cannot be avoided given the scarcity of inter-slide stratigraphic correlations, such as corresponding laminae/structures; and aligning corresponding laminae between the two core logs only relocates the error to a different portion of the reconstructed core. Perhaps some of the observed offset is the result of measurement error associated with sediment deformation, but care was taken to avoid this, and the effects are assumed to be minimal. In conclusion, modest uncertainty must be considered in interpretations, but is here accepted as is: at some point between the uppermost laminae range, which is in agreement between the two stratigraphies, and the base of the middle laminae range, a cumulative ~1 cm of the thin-section record is lost and this maintains at least as deep as the pink lamina, but likely deeper. This 1-cm error ultimately has little effect on further stratigraphic, geochemical, and chronological interpretations of core D10.5, but it is important to treat the following interpretations based upon the depths of the laminae-rich portions as estimates rather than accurate values (although thicknesses of laminae-rich portions are, in fact, accurate).

Stratigraphic variation in light-colored laminae abundance is used here as a proxy for elevated lake sedimentation based on the methods of Snyder et al. (2000) and the greater lightness of cirque-affiliated sediments relative to Linnéelva sediments (Fig. 5, Table 1). Given the bathymetry and circulation patterns of Linnévatnet, the west basin is relatively isolated from the sedimentary input, including anomalous events, of Linnéelva (Svendsen et al., 1989). Therefore, the sediments comprising light-colored laminae are likely cirque-affiliated sediments and the valley-occupying marine sediments, reworked by fluvial activity associated with cirque drainage (Jansson et al., 2005).



Core D10.5 exhibits three distinct regions of abundant laminae, which suggest three episodes of elevated sedimentation. For the uppermost and lowermost laminated regions, there is good correspondence, taking offset into account, between split-core and thin-section core stratigraphy, though the lowermost region is more extensive than macroscopic observations suggest. The middle laminated region (29.5-31.8 cm) is enclosed by the range with a yellow hue, which suggests that this region contains significant amounts of the light-colored, cirque-affiliated sediments; and these stratigraphic observations are therefore considered consistent. Using the core chronology, the younger two intervals (1329-63 CE and 1816 CE-Present) are coincident with LIA intervals, while the earliest interval (984-1082 CE) falls within the timing of the MCA (Fig. 12; Grove, 1988; Mann et al., 2009).

The duration of the earliest laminated zone overlaps a period of moraine stabilization, yet coincides with the first half of the MCA (Fig 12; Werner, 1993). The elevated local summer air temperatures concurrent with this period and the relative warmth in the North Atlantic during the MCA suggest that glaciation in the west basin cirque was unlikely during this time (D'Andrea et al., 2012; Lamb, 1977; Mann et al., 2009). However, the occurrence of light-colored laminae, which is assumed here and in Snyder et al. (2000) to represent cirque glacier advance in this system, is surprising during a period with a deglaciated cirque. The increased abundance of light-colored laminae in this interval may represent a period of substantially increased erosion and transport of nonglacial sediments from the western valley wall and cirque drainage into the Linnévatnet west basin, driven by the elevated precipitation of a persistently positive North Atlantic Oscillation (NAO) during the MCA (Fig 12; Olsen et al., 2012; Trouet et al., 2009). Under these elevated precipitation conditions, increased snow accumulation on the cirque and valley walls would generate increased spring meltwater, which might mimic the erosive processes of glacial meltwater. It is not uncommon for sedimentary layers derived from erosive slope processes to resemble similar glacigenic laminae in lacustrine sediments (Karlén and Matthews, 1992). Furthermore, these sediments are derived from the marine sediments of the valley bottom and the same bedrock source as the glacigenic sediment and therefore exhibit lithologies identical to sediments of the cirque and cirque drainage.

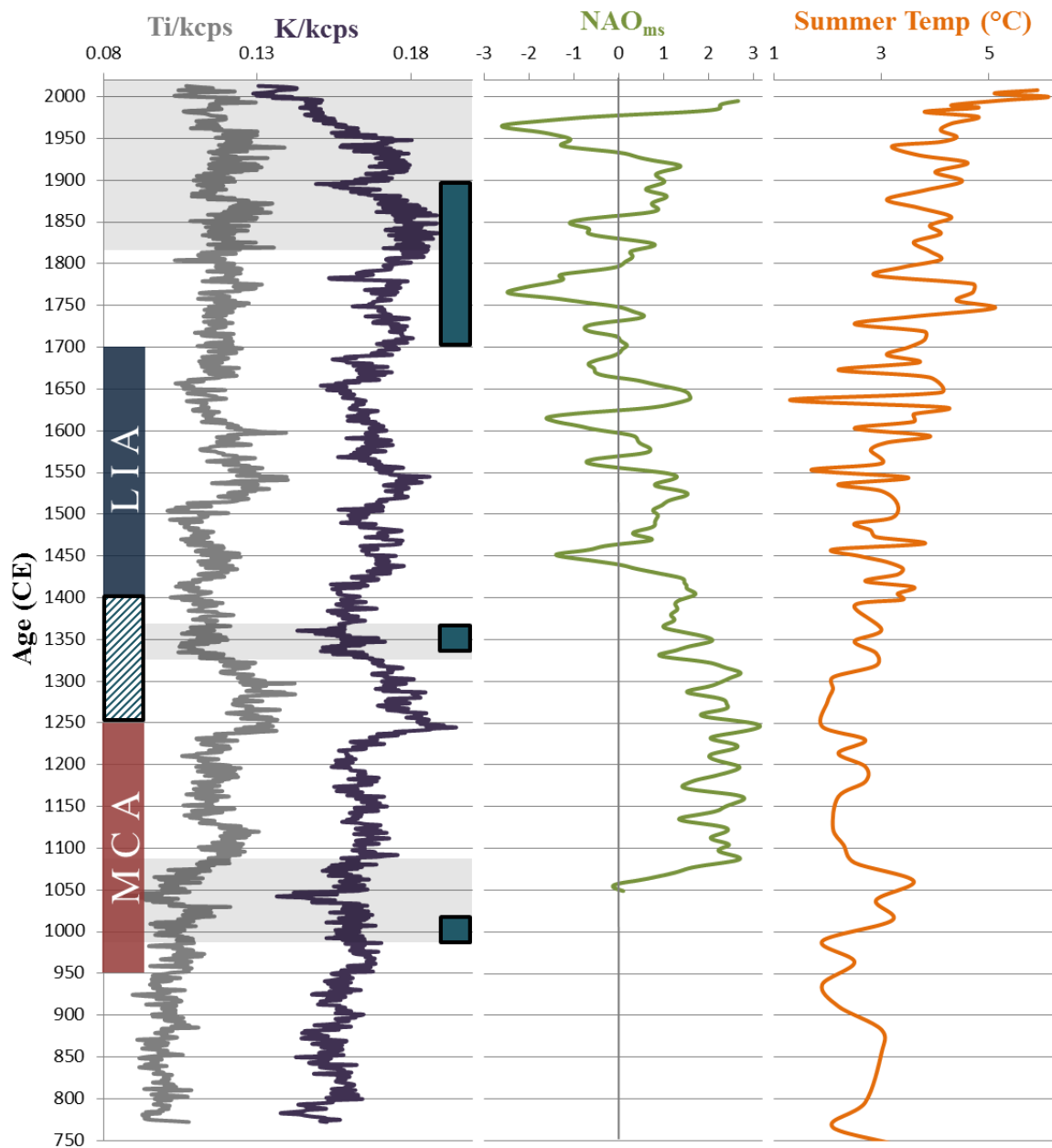


**Figure 12** Profiles of XRF-measured K and Ti (measured in peak area and normalized by kilocounts per spectrum) plotted against the age-model of core D10.5, with intervals of abundant, light-colored laminae indicated by the shaded regions. Superimposed on the K/kcps and Ti/kcps plot are periods of moraine stabilization on Spitsbergen (teal rectangles; Werner, 1993), as well as the duration of the Medieval Climate Anomaly (MCA), Little Ice Age (LIA), and intervening transitional period (box with horizontal bars), as described by Mann et al. (2012). The transitional period is typically associated with early LIA conditions (e.g. Grove, 1988). Plotted for comparison are the winter NAO index reconstruction (green) of Trouet et al. (2009) and the Kong-B June-July-August air temperature reconstruction for Kongressvatnet (orange; D’Andrea et al., 2012).

The coincidence of the two upper laminated intervals within the LIA suggests two periods of active glacial erosion and sediment delivery associated with these two periods. These findings extend those of Snyder et al. (2000), who, using a lamination index, concluded that there was only one glacial episode beginning approximately 400 yr BP. Given the relative thinness of the two lower laminae-rich zones and the macroscopic subtlety of the middle laminated section, it is possible that the 2.5 cm core intervals, within which Snyder et al. (2000) measured percent occurrence of laminae, were not sensitive enough to identify the elevated laminae frequency in these regions. Although the stratigraphy of core D10.5 could not be carefully compared with the cores studied by Snyder et al. (2000), the uppermost laminae range of core D10.5 likely corresponds with the upper coarse-laminated section observed in their cores.

With respect to the timing of the younger interval of Late Holocene cirque glaciation, the date of onset estimated in this study is 200 yr later than the date reported by Snyder et al. (2000); however given uncertainties of their radiocarbon ages, the actual onset date may be younger than the study reported. Despite downcore uncertainties with respect to sedimentation rates and depths, the uppermost laminae-rich section of core D10.5 is in fact the best constrained by direct chronological measurements and its extent is in close agreement between both visual stratigraphic analyses. For these reasons, I conclude that the timing of this interval is well supported by the results. Perhaps the later appearance of laminae in the distal west basin instead indicates when glacial erosion, sediment availability, and/or meltwater activity reached levels sufficient for transport to the shore-distal core D10.5 site. This interpretation is consistent with the findings of older glacigenic laminations in more shore-proximal cores and evidence for spatial variability in the occurrence of laminae in the west basin (Snyder et al., 2000). Karlén and Matthews (1992) assert that the presence of glacigenic layers may indicate glacial activity above a certain threshold, rather than just the presence of a glacier. This activity might include increased meltwater flux or ice that is sufficiently thick to develop localized temperate bed conditions and increase subglacial erosion (Jansson et al., 2005). With increasing sediment concentration, underflows and turbidity flows propagate to greater lateral extents (Middleton, 1967). Therefore, with increasing sediment delivery from the west basin cirque, there will be greater avalanching and slumping of delta

materials, allowing more sediment to be transported more frequently into the west basin from the cirque drainage inflow and associated delta (Church and Gilbert, 1975). Sediment-laden meltwater might also be deposited in the west basin by suspension settling from interflows. Thus, as the cirque glacier grew and began to generate and transport more sediment, more glacial material was delivered to and deposited in increasingly distal portions of the basin. However, at lower levels of glacial activity, sediment delivery to the west basin is insufficient to generate sufficiently extensive underflows or interflows of cirque-associated sediments. In conclusion, during the late-LIA, glacial advance in the west basin cirque began as early as 1400 CE and growth continued until at least 1816 CE (Figs. 10, 12; Snyder et al., 2000). Around 1816 CE, sufficiently active glacial and meltwater erosion, or ice-margin retreat and sediment exposure, provided enough sediment-laden drainage to the Linnévatnet west basin for formation of light-colored laminae (Karlén and Matthews, 1992). The visual stratigraphy alone does not inform the relative contributions of decreasing summer temperature and increasing winter precipitation on cirque glacier advance during the late LIA, but these results strongly evidence favorable conditions for cirque glacier advance during this time.

The comparatively brief (~34 yr) period, indicated by laminated sediments between 29.5 and 31.8 cm depth, likely represents only the duration of glacier maximum stand or the initial retreat of early LIA glaciation, rather than the full duration of glacial advance during the early LIA. Instead, the erosive activity of this advance was probably too modest to mobilize large amounts of sediment with meltwater, and only after moraine deposition and during subsequent retreat were sufficient volumes of sediment exposed and reworked by meltwater to generate distinct laminae in the west basin (Blass et al., 2003; Karlén and Matthews, 1992). In support of this interpretation, the timing of sedimentation coincides with a period of lesser, early LIA moraine stabilization in Spitsbergen (Werner, 1993). Furthermore, the timing corresponds with the beginning of a local warming trend from early-LIA low temperatures, which would stimulate ice margin retreat and paraglacial erosion (Fig 12; D'Andrea et al., 2012). Elevated precipitation during the concurrent positive-NAO mode might have further promoted erosion (Fig. 12; Trouet et al., 2009). This LIA advance yielded glaciation in the west basin cirque large enough to slowly erode sediment, but significant transport of sediment

to the west basin apparently occurred only during a period of moraine stabilization and/or ice retreat and paraglacial erosion between 1329-1363 CE.

### *Geochemistry and Physical Parameters*

#### Source Sediment Interpretations

Analysis of the physical parameters and geochemistry of source sediments yields a number of interpretations and considerations for source sediment XRF signal,  $L^*$ , and magnetic susceptibility characteristics. Firstly, the results of the Carbonate sample and the carbonate sediments in general are largely ignored due to the poor sample quality (large grain size and contamination) and the relative isolation of the west basin from the carbonate sediment source (Svendsen et al., 1989). Furthermore, the data indicate that the carbonate sediment is not characteristically enriched in any of the observed elements or parameters, except  $L^*$ , so influence of carbonate sediment is unlikely to be observed definitively in the XRF profiles with sufficiently high signal-to-noise ratios. Secondly, Marine Mud values ought to be considered with slight caution due to the presence of mollusc shell fragments, but care was taken to remove these and associated errors are unlikely, albeit possible.

Given the high Ti signal of the Cirque, Old Fan, and Active Channel samples, elevated Ti signal is interpreted to be indicative of increased cirque-associated sediment content in core D10.5. Similarly, values of  $\kappa$  and Fe are highest for Marine Mud, so variations of these values in core D10.5 are typically assumed to reflect changes in marine sediment content. The K signal in the XRF record is considered a proxy for cirque-associated sediments and marine sediment, given higher values in these four sediment types. Cirque-associated and marine sediments are expected to typically be mixed together in the west basin record because cirque meltwater drainage has flown through extant valley sediments and likely reworked and transported these, along with cirque sediments, into the west basin of Linnévatnet (Jansson et al., 2005). The mixing of cirque-derived sediments with the marine sediments of Linnédalen is further supported by the elevated values of  $\kappa$ , Fe, and Mn in the Old Fan sediments, which were previously carried, reworked, and deposited by cirque meltwater (Snyder et al., 2000). Finally,

Linnéelva sediment exhibits the lowest  $L^*$  value, so low  $L^*$  values are associated with increased proportions of Linnéelva sediment.

#### Comparison of XRF and ICP-MS Profiles

In core D10.5, high signal-to-noise ratios are observed in K, Ti, and Fe, a finding consistent with a similar ITRAX XRF-based study of lacustrine sediments (Cuven et al., 2010). However, Cuven et al. (2010) stress that the XRF data from ITRAX core scans are only semi-quantitative, as the measurements can be influenced by various characteristics of the sediment, such as interstitial water content (Tjallingii et al., 2007). On the other hand, the discrete ICP-MS samples provide quantitative measurements of sediment elemental composition. Mn and Fe XRF profile trends are in agreement with the trends in respective coarse-resolution ICP-MS profiles, while Ti and K show markedly different downcore trends in ICP-MS data relative to XRF data.

ICP-MS profiles were also normalized with Al, which is customarily used as a lithogenic reference element to calculate enrichment factors of other elements (Boës et al., 2011). ICP-MS profiles of Fe and Mn, regardless of Al-normalization, correspond well with XRF profiles and for that reason, these XRF profiles are considered to be representative, though not absolutely quantitative measurements, of downcore trends in Fe and Mn. In contrast, non-normalized ICP-MS values of Ti only vary between the two values 0.002% and 0.003% (Fig. 11). In result, the %Ti profile of core D10.5 offers little insight into the nuanced variation of Ti content in core D10.5, while the Al-normalized profile is dominated by variations in Al. With respect to K, values of %K are well-correlated with those of %Al ( $r^2=0.91$ ) for core D10.5 sediments, and this high correlation yields an approximately constant K/Al profile (See Appendix). Therefore, XRF profiles of Ti and K are clearly not well-representative of actual sediment geochemistry, and for that reason, all subsequent interpretations of Ti and K XRF profiles must be considered with caution. However, the distinct Ti and K XRF signals of cirque-associated sediments and marine sediment in the valley suggest that these data are useful proxies of relative source sediment proportions.

## Sustained Changes in Colorimetric Lightness and Ti/kcps

Two sustained changes are observed in the geochemical and physical stratigraphy of core D10.5 that correspond with ranges of increased laminae abundance. A dramatic decrease in  $L^*$  occurs across the middle laminae-rich region, indicative of an increased proportion of low- $L^*$  Linnéelva sediment in the west basin record. However, this is unexpected during a period of cirque glaciation since enhanced erosion of the high- $L^*$  cirque sediments and marine sediments should result in an increased  $L^*$  for the sediment record. Instead, results suggest that there was a net increase of fine, coal-rich Linnéelva sediments, rather than cirque-derived sediments, deposited at the core site. While at first seeming to contradict an interpretation of cirque glacier advance during this interval, the results may nonetheless be consistent with enhanced glacial and meltwater erosion in Linnédalen. During the LIA, Linnébreen advanced to its greatest extent of the Holocene, generating and transporting more sediment to Linnévatnet via Linnéelva (Svendsen and Mangerud, 1997; Werner, 1993). Even though relatively little Linnéelva sediment is carried to the west basin by lake circulation, there would nonetheless be an increase in the net influx of fine, coal-rich sediment from Linnébreen and Linnéelva to the lake overall (Mangerud and Svendsen, 1990; Svendsen and Mangerud, 1997). This may be sufficient to reduce sediment  $L^*$ , even with the concurrent elevated influx of lighter, cirque-derived sediments. The subsequent increase in  $L^*$  across the upper 6 cm (~1905 CE-Present) of core D10.5 corresponds initially with increasing Ti XRF signal in core D10.5 (6-3 cm depth) and likely represents a relative reduction in sediment delivery from Linnéelva. This time period overlaps a period of reduced coal mass in a core from the Linnévatnet north basin, and therefore represents a reduction in sediment delivery from Linnévatnet and/or an increase in cirque-derived sedimentation across Linnévatnet (Pompeani, 2009). Ultimately, the  $L^*$  profile of core D10.5 indicates an increase in glacial sediment production and deposition in Linnévatnet throughout the LIA and perhaps a slight reduction within the last century.

The second, more subtle geochemical change with laminae abundance is a shift in mean Ti XRF signal within the lowest (MCA) laminae range to an elevated mean value that is sustained upcore. This is interpreted as the signal of a sustained increase in erosive activity from elevated precipitation (MCA) and later glaciation (LIA) on western valley

wall and cirque sediments in Linnédalen, resulting in increased deposition of Ti-enriched sediments in the Linnévatnet west basin. While this does not necessarily indicate a change in cirque glacier activity, it suggests that elevated erosive activity yielded a substantial increase in the transport of sediment from the western valley walls and deposition in the west basin, beginning with elevated precipitation during the MCA. Within this overall shift, there are more subtle variations in Ti signal, which may be linked to glaciological and hydrological processes in Linnédalen.

Aside from the two aforementioned observations, stratigraphic variations in XRF signals and physical parameters do not exhibit substantial, sustained changes in sediment character during or following periods of glacial activity (as indicated by abundant light-colored laminae). Rather, profiles of magnetic susceptibility and XRF geochemistry suggest that west basin sediment chemistry and character is complexly related to erosive and depositional sedimentary processes in Linnédalen and Linnévatnet. These processes and their proxies are further complicated by the various interactions between cirque- and valley wall-derived sediments and the valley-occupying marine sediments.

#### Fluctuations in Ti/kcps and K/kcps

The similar XRF profiles of Ti and K, the relatively high correlation between their XRF values ( $r^2=0.37$ ; See Appendix), and their co-enrichment in cirque sediments suggest a similar provenance for Linnévatnet sediments with elevated Ti and K signals. The subtle differences in these profiles, particularly the very subtle K lags and the isolated K minimum, are best explained by variation in grain geochemistry, whereby Ti is relatively enriched in coarser sediments and K and Fe are enriched in finer sediments (Cuven et al., 2010). Under this interpretation, slightly-coarser Ti-enriched grains settle out first, followed by the finer K-enriched grains, but it is important to note that this is only relevant for microscopic lags, such as those observed at ~44.05 cm and 35.4 cm depth. Conversely, larger differences between K and Ti curves, such as the 1.9 cm lag between minima in the upper laminae portion of core D10.5, are too great to be accounted for by this subtle settling process and are likely linked to differential input of different source sediments or sediment sizes. For instance, the isolated K minimum (13.65 cm) corresponds with a small increase in Fe, and so this may represent a



particularly fine-grained event or perhaps an event characterized exclusively by the Fe- and K-enriched (but Ti-deficient) marine sediment, such as a slump of littoral sediment.

Relative Ti- and K- enrichment of cirque-affiliated sediments suggest that periods of increased cirque-derived sedimentation should correlate with increased Ti and K signals, but rather, these intervals are associated with gradual increases interrupted by abrupt decreases in the signals. Such fluctuations in Ti and K during the glacial intervals may be due to decadal-scale advance and retreat of the cirque glacier ice margin (Leonard, 1997). Retreat exposes increasing amounts of glacial sediment, leading to gradual increases in Ti and K in the west basin record, while depletion of this sediment or glacial readvance over sediment results in the relatively rapid decreases (Blass et al., 2003; Karlén and Matthews, 1992). Alkenone-based summer temperatures reconstructed from the sediments of a nearby lake (Kongressvatnet) oscillate on approximately decadal scales over the course of these periods (Fig. 12; D'Andrea et al., 2012). Such oscillations may be driving glacial advance and retreat in the west basin cirque during these periods. Alternatively, fluctuations in Ti and K during these glacial intervals may be driven by changes in precipitation regime and its effect on runoff and erosion, whereby increased precipitation yields greater runoff and increased transport of cirque-derived sediments to the west basin. Fluctuations of Ti and K signal in the earlier interval (1329-1363 CE) are in-phase with NAO mode fluctuations, but no clear covariation is observed in the more recent interval (1816 CE-Present; Fig. 12; Trouet et al., 2009). A combination of fluctuations in ice extent and changes in precipitation, with the latter more effective during the early LIA interval and the former more effective during the late LIA interval, may provide the best explanation for these fluctuations in Ti and K signal.

Regardless of the mechanism driving fluctuations in Ti and K XRF signal, it remains unclear why there are not sustained increases in Ti and K over the laminae-rich regions or over most of the light-colored laminae when these laminae are supposedly comprised of sediments that exhibit elevated Ti and K XRF signatures. In the uppermost laminae region, which corresponds well between the thin-section and visual core-half records, a particularly distinct laminae observed in the thin-section record at ~5.8 cm depth corresponds with a local maxima in Ti at approximately that same depth. However, this is not the case for fainter laminae and laminae further downcore, which do not appear

to correspond well with K/Ti peaks. One important consideration is the uncertainty in correlating depths from the reconstructed thin-section D10.5 record with depths from the corresponding core-half surface, which may account for the apparent lack of correspondence between downcore laminae and K/Ti peaks. Also, fainter laminae, which are both relatively thinner and typically exhibit a more muted color, may not generate distinct Ti or K signals because of mixing with Linnéelva-derived sediments during transport and deposition in the west basin. The relative thinness of these laminae indicates deposition by inflows of reduced sediment volume and/or concentration. With reduced sediment concentration, river inflows are more prone to form interflows rather than underflows in a lacustrine environment, and the sediment would then deposit in the west basin by suspension settling (An, 2011; Francus et al., 2008). During the course of suspension settling in the west basin, fine-grained Linnéelva-derived sediment could be readily incorporated and settle with the interflow material derived from the cirque and cirque drainage. This mixing with Ti-/K-deficient, darker sediment would produce both a more muted color and a muted Ti or K signal in the thinner laminae. Thin laminae with more pronounced light color are expected to contain relatively little Linnéelva sediment and therefore were likely deposited by underflows and involved brief and little sediment settling from higher in the water column. A final consideration is that, although better-defined laminae are  $>0.5$  mm in thickness, thinner laminae are  $\leq 0.5$  mm in thickness. In comparison, the XRF measurement interval is 0.5 mm, and so fainter laminae may be missed or only partially measured, resulting in a reduced or absent peak in association with those thicknesses. Higher resolution ITRAX XRF analysis and a better understanding of the hydrological characteristics of drainage inflow into the west basin may provide insight into considerations of how laminae correspond with geochemical data.

An explanation based on regional glacial activity noted in other studies cannot be used to explain K and Ti fluctuations during the earliest, nonglacial interval of cirque-sediment-associated sedimentation. The MCA range is characterized by single, sudden minima in K and Ti, which coincide with an abrupt Fe maximum (in fact the maximum Fe XRF signal in core D10.5). The peak depths lie within the one region of orange mottling that was observed immediately following core splitting. The observed

geochemistry of K and Ti deficiency with high Fe-enrichment may be explained as the result of the X-ray beam striking one of the orange mottles, which are identified as regions of oxidized Fe on the split-core surface. Given the interpreted post-collection nature of the orange mottling, these geochemical variations are not indicative of changes in west basin sedimentation (König et al., 2000).

Outside of the laminae-rich ranges, fluctuations in Ti and K are consistent with, and likely related to, shifts in precipitation driven by the NAO, whereby positive NAO conditions exhibit increased precipitation, which yields increased sediment erosion (Fig. 12). The concurring Ti and K peaks at 22.7cm depth (1542 CE) coincide with positive NAO conditions, while a K peak at 15.5 cm depth (1732 CE) coincides with a very brief period of slightly positive NAO (Fig 12; Trouet et al., 2009). This isolated K peak and the corresponding slight positive NAO interval are consistent with the interpretation that slightly elevated precipitation and associated erosion would only transport relatively finer, K-enriched fractions of sediment to the distal portions of the west basin. In addition to these variations, Ti signal increases rapidly, lagged slightly by K (likely due to grain settling differences during the depositional events), at 35.4 cm depth (1234 CE). These patterns may record the increasing erosion of cirque-derived sediments and reworking of marine sediments by meltwater during the initial glacial advance of the LIA as well as continued erosion of sediments by high precipitation associated with a positive NAO, which persisted through this time interval (Fig 12; Trouet et al., 2009; Werner, 1993). In this case, glacial and meltwater activity were apparently insufficient to generate distinct laminae in the west basin, but fine-grained material was carried out in suspension or in weak inter- and underflows, and thus appears in the geochemical record.

#### Variations in Fe/kcps and Magnetic Susceptibility

Compared to K and Ti, XRF-derived values of Fe and Ti are less well correlated ( $r^2=0.28$ ), and there is particularly poor correlation between Fe and K ( $r^2=0.02$ ). The main dissimilarity between Fe and both Ti and K occurs below the middle laminae-rich range, across which Fe first increases quickly and then shows a gradually decreasing trend. Above this laminae Fe varies subtly but similarly with Ti and K. Here, I hypothesize that the Fe signal below 34 cm depth in core D10.5 is predominantly affected by changes in

the erosion of the valley bottom marine sediments over the course of the MCA. Higher precipitation rates and warmer temperatures during the positive NAO conditions of the MCA would have enhanced rain and snowmelt runoff in Linnédalen (Mann et al., 2009; Trouet et al., 2009). Fluvial erosion of the steep rivulets of the western valley walls would likely be more effective and mobilize more sediment than the fluvial erosion of the gentler sloped valley bottom near the southwestern shore of Linnévatnet. Therefore, evidence of changes in valley wall erosive processes are expected to be more pronounced in the west basin record during this period. Initially, the runoff from the steep rivulets would readily erode coastal marine sediments at the base of the valley walls along with the pelitic sediments from further upslope. The rapid increase in Fe signal at 53 cm depth (~840 CE) might represent such an increase in the transport of the marine sediments into Linnévatnet. Over time, however, exhaustion of easily erodible marine sediments at the base of the valley wall might reduce the relative amount of marine sediment delivered to Linnévatnet. Additionally, coarser material that is carried down the steep rivulets, but is too large to be carried across the valley bottom into Linnévatnet, would deposit at the base of the steep valley slopes, accumulating atop the marine sediment and perhaps armoring it from further erosion. Thus, the gradual deposition of valley wall sediment and the reduction of exposed, easily erodible marine sediment might account for the gradually declining Fe signal across the MCA. With the onset of the LIA, glacial advance in the west basin cirque yielded high-energy meltwater drainage, which was considerably more erosive than the snowmelt and rainfall runoff in the rivulets and thus dominated the sedimentary signal in the Linnévatnet west basin. This cirque glacier meltwater reworked and eroded the marine sediments in the cirque drainage area (including the associated fan), mobilizing marine sediment in proportional amounts to cirque-derived sediments from the glacier and moraine. In result, fluctuations in Fe, which is most enriched in the marine sediments, follows approximately the variations in Ti and K throughout the west basin sediment record above the onset of the LIA.

Large peaks in magnetic susceptibility and Fe precede the early-LIA laminae range at 33 cm depth. The peak in magnetic susceptibility may represent an especially large clast within the sediment at that depth, but taken with the Fe peak, the peaks are more likely related to the distinctively coarser-grained (coarse-silt to fine sand) yellow

laminae observed at that depth. The light-color of the lamina corresponds with a high  $L^*$  value which, in conjunction with the high Fe content, suggest that this sediment was derived from the bedrock of the western valley walls. However, there are no corresponding peaks in Ti and K in this sediment, and the magnetic susceptibility is surprisingly large in magnitude for a fairly subtle change in grain size. This may be explained by post-depositional, diagenetic enrichment of this lamina in ferric compounds, precipitated by groundwater flow. Groundwater would more readily flow through this layer, since sediment permeability increases with increasing grain size (Shepherd, 1989). Precipitation of ferric compounds (ex. magnetite and iron oxide-hydroxides) from solution in this layer may account for yellow color and the concurrent peaks in Fe and magnetic susceptibility (Cohen, 2003). This hypothesis, however, needs further support from quantitative measurements of  $Fe^{3+}$  content and grain size across core D10.5, with special attention to this lamina. Nonetheless, the relative coarseness of the sediment indicates that this laminae likely formed from a particularly high-energy event in the west basin, carrying material as an underflow or turbidity current (Church and Gilbert, 1975). There is no apparent evidence of erosion or disconformity between this laminae and underlying sediment, but high-energy turbidity current events, such as this, may erode into and disturb underlying sediment (Bouma, 1962; Cuven et al., 2011)

Finally, in the uppermost laminae, which represent the later LIA advance, there are decreasing upcore trends in Fe and magnetic susceptibility (starting at ~12.3 cm depth) followed by upcore decreases in K and Ti beginning at ~3 cm depth. Decreases in Fe and magnetic susceptibility are probably the result of an increased influx of cirque-derived sediments, which are slightly less Fe-rich and have lower  $\kappa$  than marine sediments, due to cirque glacier advance, moraine stabilization, and subsequently increased glacigenic sedimentation (Leonard, 1997; Ohlendorf et al., 1997). The later upcore decreases in Ti, K, and the continued decreases in Fe and  $\kappa$  are interpreted as the record of a reduction of both glacigenic sediment production/transport and marine sediment entrainment and delivery to the Linnévatnet west basin, resulting from reduced glacial erosion and meltwater activity as the cirque glacier, along with all glaciers on Spitsbergen, retreated over the course of the last century (Werner, 1993). With respect to reducing marine sediment entrainment, the modern channel sediments have lower Fe, K,

and  $\kappa$  values relative to the meltwater fan sediments, and perhaps this is a result of the channel becoming relatively stabilized in its modern position and no longer eroding, reworking, and mixing as much of the marine sediment lining its banks with cirque-derived sediment. Reducing the magnitude and frequency of high flows is associated with reduced channel migration (Shields et al., 2000). Therefore, as the cirque glacier shrank and its spring melts reduced in magnitude and frequency, migration rates of the cirque drainage channel have likely decreased as well, resulting in less erosion into the marine sediments that comprise much of the bank sediments. In addition to this process, a shift to an NAO negative mode during this range may also be contributing to reduced discharge and erosion (Trouet et al., 2009).

#### Variation in Mn/kcps

In addition to the high signal-to-noise variations in Ti, K, and Fe, this study found a high signal-to-noise Mn profile that bears implications for the sedimentary and limnological history of Linnévatnet. The XRF profile of Mn does not show any appreciable variation across the length of core D10.5, excepting two pronounced peaks and a region of elevated signal with a very large central peak. The largest peak in Mn (~33 cm depth) is a full order of magnitude greater than the most Mn-enriched source sediment (Marine Mud). The pronounced nature of these Mn peaks is mysterious, and similarly anomalous peaks in Mn are observed in cores from northern portions of the large Linnévatnet north basin, suggesting that these may represent lake-wide events (Eidmann, J., and Balter, A., pers. comm., 2014). One possible interpretation is that these peaks are associated with large inputs of marine mud, perhaps by slumps of littoral sediment, but this is unlikely given the dramatically lower XRF signal of the measured source sediments. Alternatively, these peaks may come from the influx of highly Mn-rich sediments of some yet-unconsidered sediment source, such as the karstified carbonate rocks or snowmelt and groundwater-fed alluvial fan of the eastern valley wall (Åkerman, 1983; Snyder et al., 2000). A final consideration is that these Mn spikes are associated with changes in lake redox conditions and subsequent changes in Mn solubility. Perhaps unstable climate and cold summer temperatures during the MCA-LIA transition in the 13<sup>th</sup> century promoted lake ice persistence and a reduction of lake mixing in Linnévatnet,

eventually yielding anoxic bottom conditions. Interestingly, the timing of the 17.4 cm Mn peak (ca. 1687 CE) and the 37.5-33.4 cm high-Mn-range (ca. 1192-1300 CE) correspond approximately with periods of anomalous, decreased summer temperatures at this location, and the peak at ~30 cm depth corresponds with early LIA glaciation (D'Andrea et al., 2012). As climate stabilized in the LIA and/or summer temperatures warmed, holomictic conditions would have returned, and the exposure of sediments to oxygenated water would have promoted precipitation and storage of Mn in the lacustrine sediment (Camill et al., 2012; Kylander et al., 2011). Furthermore, the dark laminae associated with this region may be an indicator of sulfate reduction and subsequent formation of dark-colored metal sulfides, although further chemical analysis with attention to sulfur is necessary to confirm this (Cohen, 2003). However, the lack of pronounced changes in Fe concurrent with these Mn events challenges the redox-change hypothesis, as concurrent increases in Fe would also be expected in such a reducing environment (Altenbach et al., 2011; Cohen, 2003). In conclusion, these Mn events need to be better characterized, but do not seem to be directly linked to glacial activity of the west basin cirque.

## **Conclusions and Future Work**

Comparison of visual, geochemical, and physical parameter stratigraphies indicate that rates and character of sedimentation in the Linnévatnet west basin have varied significantly during the course of the Late Holocene. However, sediment geochemistries measured by XRF core scans require further support from other types of quantitative analyses, as they do not reliably represent accurate sediment chemistries. Cuven et al. (2010) stress that ITRAX XRF core scans provide semiquantitative data at their best and the data must be considered as such. In particular, interpretations of K and Ti XRF profiles need to be treated with caution, while XRF profiles of Fe and Mn appear to better representative of changes in sediment geochemistry. To achieve more accurate characterization of geochemical variations in the Linnévatnet west basin stratigraphy, high-resolution quantitative techniques (e.g. ICP-MS) are required. Quantitative ICP-MS analyses were performed at a coarse resolution, but these profiles do not sufficiently capture the sub-centimeter variations that can be captured by  $\mu$ -XRF ITRAX scans and require a higher subsample frequency and resolution.

In core D10.5, the timing of climatic, glaciological, and hydrological events are extrapolated from sedimentation rates between horizons dated by  $^{239+240}\text{Pu}$  radionuclide dating and a chemostratigraphic technique based on anthropogenically increased atmospheric deposition of metals. The chemostratigraphic approach to dating the 1850 CE horizon with Hg is supported by the findings of Drevnick et al. (2012), and local coal burning sources support the interpretation of increased Cr and Ba deposition in coal ash from Barentsburg beginning ca. 1932 CE. An age-depth model based on  $^{239+240}\text{Pu}$  radionuclide and chemostratigraphic horizons was developed to determine approximate age intervals of elevated sedimentation, but more precise absolute dating techniques are required to improve these estimates. Radiocarbon dates in lower core portions, and/or stratigraphic correlation with radiocarbon-dated cores such as those studied by Snyder et al. (1994, 2000) may yield more accurate sedimentation rates as well as additional downcore ages, although recovery of suitable material for radiocarbon chronologies may be difficult.

Ultimately, stratigraphic and geochemical variations in the lacustrine record of the Linnévatnet west basin indicate that sedimentation in this system has been more sensitive to climatological change than previously thought (Snyder et al., 1994, 2000). Visual stratigraphy of the west basin record indicates advances of the cirque during both periods of LIA glacial advance in Spitsbergen (Werner, 1993). Geochemistry of the Linnévatnet sediment record within stratigraphic ranges of LIA deposition provides evidence of possible decadal-scale fluctuations of the cirque glacier ice margin during these advances or perhaps changes in precipitation and runoff conditions driven by variation in NAO mode. Differences between these findings and those of Snyder et al. (2000) may be accounted for by differences in analytical stratigraphic techniques as well as spatial variation in the west-basin record resultant from weaker erosion and meltwater sediment transport during early glacial advance. Careful comparison with more shore-proximal cores and cores from other regions of the west basin may provide more precise timing estimates of cirque glacier advance during the LIA.

In addition to glacial advances, this study found evidence of a period of elevated sedimentation during the MCA, likely driven by corresponding increases in precipitation (Trouet et al., 2009). Furthermore, geochemical fluctuations during this and other non-



LIA time periods appear well-associated with fluctuations in the NAO and may perhaps be driven by the effects of changing precipitation rates on Linnédalen hydrology. Overlain upon these geochemical variations are stratigraphic variations in Mn that evidence either complex limnological processes regulating the mobility of Mn in Linnévatnet sediments or input from an unaccounted for sedimentation source.

In conclusion, the lacustrine environment of the proglacial Linnévatnet is strongly influenced by the complex hydrological and glaciological processes of Linnédalen, and perhaps limnological processes as well. To determine more accurately how cirque glaciation in Linnédalen has changed through the Late Holocene, the small-scale hydrological processes acting on the western valley slopes and their drainage networks into Linnévatnet need to be better characterized. Nonetheless, there is strong evidence that this small cirque glacier in western Spitsbergen was quite sensitive to climatic shifts, and even milder early-LIA conditions were sufficient to drive cirque glaciation in Linnédalen.

## References

- Altenbach, A. V., Bernhard, J. M., and Seckbach, J., 2011, Anoxia: Evidence for Eukaryote Survival and Paleontological Strategies, Springer Science.
- An, S. D., 2011, Interflow dynamics and three-dimensional modeling of turbid density currents in Imha reservoir, South Korea: Colorado State University.
- Baranowski, S., and Karlén, W., 1976, Remnants of Viking Age Tundra in Spitsbergen and Northern Scandinavia: *Geografiska Annaler. Series A, Physical Geography*, v. 58, no. 1, p. 35-40.
- Berg, T., and Steinnes, E., 1997, Recent trends in atmospheric deposition of trace elements in Norway as evident from the 1995 moss survey: *Science of The Total Environment*, v. 208, no. 3, p. 197-206.
- Björnsson, H., Gjessing, Y., Hamran, S.-E., and Hagen, J. O., 1996, The thermal regime of sub-polar glaciers mapped by multi-frequency radio-echo sounding: *Journal of Glaciology*, v. 42, no. 140, p. 23-32.
- Blake, W., 2006, Occurrence of the *Mytilus edulis* complex on Nordaustlandet, Svalbard: radiocarbon ages and climatic implications: *Polar Research*, v. 25, no. 2, p. 123-137.
- Blass, A., Anselmetti, F. S., and Ariztegui, D., 2003, 60 years of glaciolacustrine sedimentation in Steinsee (Sustenpass, Switzerland) compared with historic events and instrumental meteorological data: *Eclogae geologicae Helvetiae*, v. 96, p. S59-S71.
- Boës, X., Rydberg, J., Martinez-Cortizas, A., Bindler, R., and Renberg, I., 2011, Evaluation of conservative lithogenic elements (Ti, Zr, Al, and Rb) to study anthropogenic element enrichments in lake sediments: *Journal of Paleolimnology*, v. 46, no. 1, p. 75-87.
- Bouma, A. H., 1962, *Sedimentology of some Flysch deposits; a graphic approach to facies interpretation*, New York, Elsevier Publishing Co.
- Bøyum, A., and Kjensmo, J., 1978, Physiography of Lake Linnévaten, western Spitsbergen: *Verhandlungen des Internationalen Verein Limnologie*, v. 20, p. 609-614.
- Camill, P., Umbanhowar, C., Jr., Geiss, C., Hobbs, W., Edlund, M., Shinneman, A., Dorale, J., and Lynch, J., 2012, Holocene climate change and landscape development from a low-Arctic tundra lake in the western Hudson Bay region of Manitoba, Canada: *Journal of Paleolimnology*, v. 48, no. 1, p. 175-192.
- Church, M., and Gilbert, R., 1975, Proglacial fluvial and lacustrine environments, in Jopling, A. V., and MacDonald, B. C., eds., *Society of Economic Paleontologists and Mineralogists Special Publication No. 25*.

- Cohen, A. S., 2003, *Paleolimnology: The history and evolution of lake systems*, New York, Oxford University Press.
- Cuven, S., Francus, P., and Lamoureux, S., 2010, Estimation of grain size variability with micro X-ray fluorescence in laminated lacustrine sediments, Cape Bounty, Canadian High Arctic: *Journal of Paleolimnology*, v. 44, no. 3, p. 803-817.
- Cuven, S., Francus, P., and Lamoureux, S., 2011, Mid to Late Holocene hydroclimatic and geochemical records from the varved sediments of East Lake, Cape Bounty, Canadian High Arctic: *Quaternary Science Reviews*, v. 30, no. 19–20, p. 2651-2665.
- D’Andrea, W. J., Vaillencourt, D. A., Balascio, N. L., Werner, A., Roof, S. R., Retelle, M., and Bradley, R. S., 2012, Mild Little Ice Age and unprecedented recent warmth in an 1800 year lake sediment record from Svalbard: *Geology*, v. 40, no. 11, p. 1007-1010.
- Debret, M., Desmet, M., Balsam, W., Copard, Y., Francus, P., and Laj, C., 2006, Spectrophotometer analysis of Holocene sediments from an anoxic fjord: Saanich Inlet, British Columbia, Canada: *Marine Geology* v. 229, p. 15-28.
- Debret, M., Sebag, D., Desmet, M., Balsam, W., Copard, Y., Mourier, B., Susperrigui, A. S., Arnaud, F., Bentaleb, I., Chapron, E., Lallier-Vergès, E., and Winiarski, T., 2011, Spectrocolorimetric interpretation of sedimentary dynamics: the new “Q7/4 diagram”: *Earth-Science Reviews*, v. 109, no. 1-2, p. 1-19.
- Dowey, C., 2013, 600 years of Late Holocene climate variability inferred from a varved proglacial sediment record Linnévatnet, Svalbard, Norway: Bates College, 66 p.
- Drevnick, P. E., Yang, H., Lamborg, C. H., and Rose, N. L., 2012, Net atmospheric mercury deposition to Svalbard: Estimates from lacustrine sediments: *Atmospheric Environment*, v. 59, p. 509-513.
- Ebbesen, H., Hald, M., and Eplet, T. H., 2007, Lateglacial and early Holocene climatic oscillations on the western Svalbard margin, European Arctic: *Quaternary Science Reviews*, v. 26, no. 15–16, p. 1999-2011.
- Eidmann, J., and Balter, A., 2014, Personal communication with honor's students at Williams College (Eidmann) and Bates College (Balter).
- Førland, E. J., Rasmus, B., Inger, H.-B., and Jan Erik, H., 2011, Temperature and precipitation development at Svalbard 1900-2100: *Advances in Meteorology*, v. 2011, no. 3, p. 1-14.
- Forman, S. L., 1990, Post-glacial relative sea-level history of northwestern Spitsbergen, Svalbard: *Geological Society of America Bulletin*, v. 102, no. 11, p. 1580-1590.
- Francus, P., Bradley, R., Lewis, T., Abbott, M., Retelle, M., and Stoner, J., 2008, Limnological and sedimentary processes at Sawtooth Lake, Canadian High Arctic,

- and their influence on varve formation: *Journal of Paleolimnology*, v. 40, no. 3, p. 963-985.
- Grove, J. M., 1988, *The Little Ice Age*, New York, Methuen.
- Guoqiang, C. H. U., Jiaqi, L. I. U., Denyi, G. A. O., and Qing, S. U. N., 2006, Mechanism of Varve Formation and Paleoenvironmental Research at Lake Bolterskardet, Svalbard, the Arctic: *Acta Geologica Sinica - English Edition*, v. 80, no. 4, p. 557-563.
- Hagen, J. O., Eiken, T., Kohler, J., and Melvold, K., 2005, Geometry changes on Svalbard glaciers: mass-balance or dynamic response?: *Annals of Glaciology*, v. 42, p. 255-261.
- Hagen, J. O., Kohler, J., Melvold, K., and Winther, J.-G., 2003, Glaciers in Svalbard: mass balance, runoff, and freshwater flux: *Polar Research*, v. 22, no. 2, p. 145-159.
- Harrison, R. M., Smith, D. J. T., Piou, C. A., and Castro, L. M., 1997, Comparative receptor modelling study of airborne particulate pollutants in Birmingham (United Kingdom), Coimbra (Portugal) and Lahore (Pakistan): *Atmospheric Environment*, v. 31, no. 20, p. 3309-3321.
- Hjelle, A., Lauritzen, Ø., Salvigsen, O., and Winsnes, T. S., 1986, Geological map of Van Mijenfjorden, Svalbard 1:100,000: Norsk Polarinstitutt.
- Hodgkins, R., 1997, Glacier hydrology in Svalbard, Norwegian high Arctic: *Quaternary Science Reviews*, v. 16, no. 9, p. 957-973.
- Humlum, O., Elberling, B., Hormes, A., Fjordheim, K., Hansen, O. H., and Heinemeier, J., 2005, Late-Holocene glacier growth in Svalbard, documented by subglacial relict vegetation and living soil microbes: *The Holocene*, v. 15, no. 3, p. 396-407.
- Jansson, P., Rosqvist, G., and Schneider, T., 2005, Glacier fluctuations, suspended sediment flux and glacio-lacustrine sediments: *Geografiska Annaler: Series A, Physical Geography*, v. 87, no. 1, p. 37-50.
- Jones, G., 1968, *A history of the Vikings*, New York, Oxford University Press.
- Karlén, W., and Matthews, J. A., 1992, Reconstructing Holocene glacier variations from glacial lake sediments: studies from Nordvestlandet and Jostedalsbreen-Jotunheimen, southern Norway: *Geografiska Annaler. Series A, Physical Geography*, v. 74, no. 4, p. 327-348.
- Ketterer, M. E., 2014, Personal communication.
- Ketterer, M. E., Hafer, K. M., Jones, V. J., and Appleby, P. G., 2004, Rapid dating of recent sediments in Loch Ness: inductively coupled plasma mass spectrometric

- measurements of global fallout plutonium: *Science of The Total Environment*, v. 322, no. 1–3, p. 221-229.
- König, I., Lougear, A., Bruns, P., Gruetzner, J., Trautwein, A. X., and Dullo, W. C., 2000, Iron oxidation in sediment cores (Site 1062) during six months of storage in the Ocean Drilling Program archive, *in* Keigwin, L. D., Rio, D., Acton, G. D., and Arnold, E., eds., *Proceedings of the Ocean Drilling Program, Scientific Results, Volume 172*.
- Kylander, M. E., Ampel, L., Wohlfarth, B., and Veres, D., 2011, High-resolution X-ray fluorescence core scanning analysis of Les Echets (France) sedimentary sequence: new insights from chemical proxies: *Journal of Quaternary Science*, v. 26, no. 1, p. 109-117.
- Lamb, H. H., 1972, *Climate: present, past and future (Volume 1: fundamentals and climate now)*, London, Methuen.
- Lamb, H. H., 1977, *Climate: present, past and future (Volume 2: Climatic history and the future)*, London, Methuen.
- Landvik, J. Y., Brook, E. J., Gualtieri, L., Raisbeck, G., Salvigsen, O., and Yiou, F., 2003, Northwest Svalbard during the last glaciation: Ice-free areas existed: *Geology*, v. 31, no. 10, p. 905-908.
- Landvik, J. Y., Ingólfsson, Ó., Mienert, J., Lehman, S. J., Solheim, A., ElverhøI, A., and Ottesen, D. A. G., 2005, Rethinking Late Weichselian ice-sheet dynamics in coastal NW Svalbard: *Boreas*, v. 34, no. 1, p. 7-24.
- Leonard, E. M., 1986, Use of lacustrine sedimentary sequences as indicators of Holocene glacial history, Banff National Park, Alberta, Canada: *Quaternary Research*, v. 26, no. 2, p. 218-231.
- Leonard, E. M., 1997, The relationship between glacial activity and sediment production: evidence from a 4450-year varve record of neoglacal sedimentation in Hector Lake, Alberta, Canada: *Journal of Paleolimnology*, v. 17, no. 3, p. 319-330.
- Leonard, E. M., and Reasoner, M. A., 1999, A Continuous Holocene Glacial Record Inferred from Proglacial Lake Sediments in Banff National Park, Alberta, Canada: *Quaternary Research*, v. 51, no. 1, p. 1-13.
- Liestøl, O., 1993, Glaciers of Svalbard, Norway, *in* Williams, R. S., Jr., and Ferrigno, J. G., eds., *Satellite image atlas of glaciers of the world: U.S. Geological Survey Professional Paper 1386-E (Glaciers of Continental Europe)*, p. E127-E151.
- Lowell, J. D., 1972, Spitsbergen Tertiary orogenic belt and the Spitsbergen fracture zone: *Geological Society of America Bulletin*, v. 83, no. 10, p. 3091-3102.

- Mangerud, J., Bolstad, M., Elgersma, A., and Helliksen, D., 1992, The last glacial maximum on Spitsbergen, Svalbard: *Quaternary research*, v. 38, no. 1, p. 1-31.
- Mangerud, J., and Svendsen, J. I., 1990, Deglaciation chronology inferred from marine sediments in a proglacial lake basin, western Spitsbergen, Svalbard: *Boreas*, v. 19, no. 3, p. 249-272.
- Mann, M. E., Zhang, Z., Rutherford, S., Bradley, R. S., Hughes, M. K., Shindell, D., Ammann, C., Faluvegi, G., and Ni, F., 2009, Global Signatures and Dynamical Origins of the Little Ice Age and Medieval Climate Anomaly: *Science*, v. 326, p. 1256-1260.
- Middleton, G. V., 1967, Experiments on density and turbidity currents: III. Deposition of sediment: *Canadian Journal of Earth Sciences*, v. 4, no. 3, p. 475-505.
- Nesje, A., Dahl, S. O., Thun, T., and Nordli, Ø., 2008, The 'Little Ice Age' glacial expansion in western Scandinavia: summer temperature or winter precipitation?: *Climate Dynamics*, v. 30, no. 7-8, p. 789-801.
- Nuth, C., Moholdt, G., Kohler, J., Hagen, J. O., and Kääb, A., 2010, Svalbard glacier elevation changes and contribution to sea level rise: *Journal of Geophysical Research: Earth Surface*, v. 115, no. F1, p. F01008.
- Ohlendorf, C., Niessen, F., and Weissert, H., 1997, Glacial varve thickness and 127 years of instrumental climate data: a comparison: *Climatic Change*, v. 36, no. 3-4, p. 391-411.
- Ohta, Y., Hjelle, A., Andresen, A., Dallmann, W. K., and Salvigsen, O., 1992, Geological map of Isfjorden, Svalbard 1:100,000: Norsk Polarinstitut.
- Olsen, J., Anderson, N. J., and Knudsen, M. F., 2012, Variability of the North Atlantic Oscillation over the past 5,200 years: *Nature Geoscience*, v. 5, no. 11, p. 808-812.
- Ooki, A., Uematsu, M., Miura, K., and Nakae, S., 2002, Sources of sodium in atmospheric fine particles: *Atmospheric Environment*, v. 36, no. 27, p. 4367-4374.
- Orheim, A., Bieg, G., Brekke, T., Horseide, V., and Stenvold, J., 2007, Petrography and geochemical affinities of Spitsbergen Paleocene coals, Norway: *International Journal of Coal Geology*, v. 70, no. 1-3, p. 116-136.
- Overpeck, J., Hughen, K., Hardy, D., Bradley, R., Case, R., Douglas, M., Finney, B., Gajewski, K., Jacoby, G., Jennings, A., Lamoureux, S., Lasca, A., MacDonald, G., Moore, J., Retelle, M., Smith, S., Wolfe, A., and Zielinski, G., 1997, Arctic Environmental Change of the Last Four Centuries: *Science*, v. 278, no. 5341, p. 1251-1256.

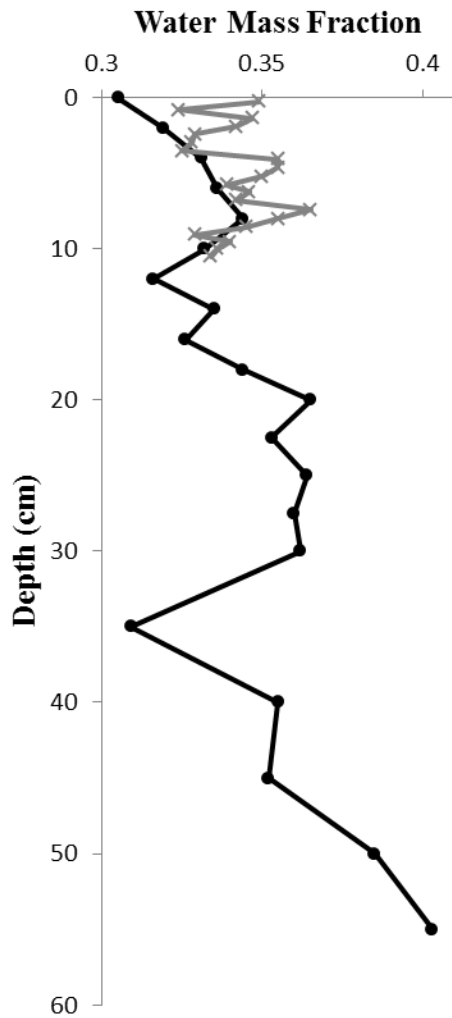
- Pfeffer, W. T., Sassolas, C., Bahr, D. B., and Meier, M. F., 1998, Response time of glaciers as a function of size and mass balance: 2. Numerical experiments: *Journal of Geophysical Research: Solid Earth*, v. 103, no. B5, p. 9783-9789.
- Pompeani, D. P., 2009, A 360 year varve-based climate reconstruction from Linnevatnet on western Svalbard: *University of Pittsburgh*, 31 p.
- Reusche, M., Winsor, K., Carlson, A. E., Marcott, S. A., Rood, D. H., Novak, A., Roof, S., Retelle, M., Werner, A., Caffee, M., and Clark, P. U., 2014, <sup>10</sup>Be surface exposure ages on the late-Pleistocene and Holocene history of Linnébreen on Svalbard: *Quaternary Science Reviews*, v. 89, no. 0, p. 5-12.
- Richter, N., 2014, Personal communication with honor's student at Northwestern University.
- Salvigsen, O., and Høgvard, K., 2005, Glacial history, Holocene shoreline displacement and palaeoclimate based on radiocarbon ages in the area of Bockfjorden, north-western Spitsbergen, Svalbard: *Polar research*, v. 25, no. 1, p. 15-24.
- Shepherd, R. G., 1989, Correlations of permeability and grain size: *Ground Water*, v. 27, no. 5, p. 633-638.
- Shields, F. D., Simon, A., and Steffen, L. J., 2000, Reservoir effects on downstream river channel migration: *Environmental Conservation*, v. 27, no. 01, p. 54-66.
- Snyder, J. A., Miller, G. H., Werner, A., Jull, A. J. T., and Stafford, T. W., 1994, AMS-radiocarbon dating of organic-poor lake sediment, an example from Linnévatnet, Spitsbergen, Svalbard: *The Holocene*, v. 4, no. 4, p. 413-421.
- Snyder, J. A., Werner, A., and Miller, G. H., 2000, Holocene cirque glacier activity in western Spitsbergen, Svalbard: sediment records from proglacial Linnévatnet: *The Holocene*, v. 10, no. 5, p. 555-563.
- Steinnes, E., and Friedland, A. J., 2006, Metal contamination of natural surface soils from long-range atmospheric transport: existing and missing knowledge: *Environmental reviews*, v. 14, no. 3, p. 169-186.
- Svendsen, J. I., and Mangerud, J., 1997, Holocene glacial and climatic variations on Spitsbergen, Svalbard: *The Holocene*, v. 7, no. 1, p. 45-57.
- Svendsen, J. I., Mangerud, J., Elverhøi, A., and Solheim, A., 1992, The Late Weichselian glacial maximum on western Spitsbergen inferred from offshore sediment cores: *Marine geology*, v. 104, no. 1-4, p. 1-17.
- Svendsen, J. I., Mangerud, J., and Miller, G. H., 1989, Denudation rates in the Arctic estimated from lake sediments on Spitsbergen, Svalbard: *Palaeogeography, Palaeoclimatology, Palaeoecology*, v. 76, p. 153-168.

- Sverdrup, H. U., 1935, Scientific Results of the Norwegian-Swedish Spitsbergen Expedition in 1934. Part III. The temperature of the firn on Isachsen's Plateau, and general conclusions regarding the temperature of the glaciers on West-Spitzbergen: *Geografiska Annaler*, v. 17, p. 53-88.
- Swift, J. H., 1986, The Arctic waters, *in* Hurdle, B. G., ed., *The Nordic Seas*: New York, Springer-Verlag, p. 129-153.
- Tjallingii, R., Röhl, U., Kölling, M., and Bickert, T., 2007, Influence of the water content on X-ray fluorescence core-scanning measurements in soft marine sediments: *Geochemistry, Geophysics, Geosystems*, v. 8, no. 2, p. Q02004.
- Tomkins, J. D., Antoniadou, D., Lamoureux, S. F., and Vincent, W. F., 2008, A simple and effective method for preserving the sediment-water interface of sediment cores during transport: *Journal of Paleolimnology*, v. 40, p. 577-582.
- Trouet, V., Valérie, T., Jan, E., Nicholas, E. G., and Andy, B., 2009, Persistent positive North Atlantic Oscillation mode dominated the Medieval Climate Anomaly: *Science*, v. 324, no. 5923, p. 78-80.
- Werner, A., 1993, Holocene moraine chronology, Spitsbergen, Svalbard: lichenometric evidence for multiple Neoglacial advances in the Arctic: *The Holocene*, v. 3, no. 2, p. 128-137.
- Worsley, D., 2008, The post-Caledonian development of Svalbard and the western Barents Sea: *Polar Research*, v. 27, no. 3, p. 298-317.
- Zamora-Reyes, D., 2011, The role of underflows and weather on sediment distribution in glacial-fed Lake Linné, Svalbard, Norway: University of Texas at El Paso, 99 p.
- Åkerman, J. H., 1983, Notes on chemical weathering, Kapp Linné, Spitsbergen, Fourth International Conference on Permafrost: Fairbanks, AK, p. 10-15.

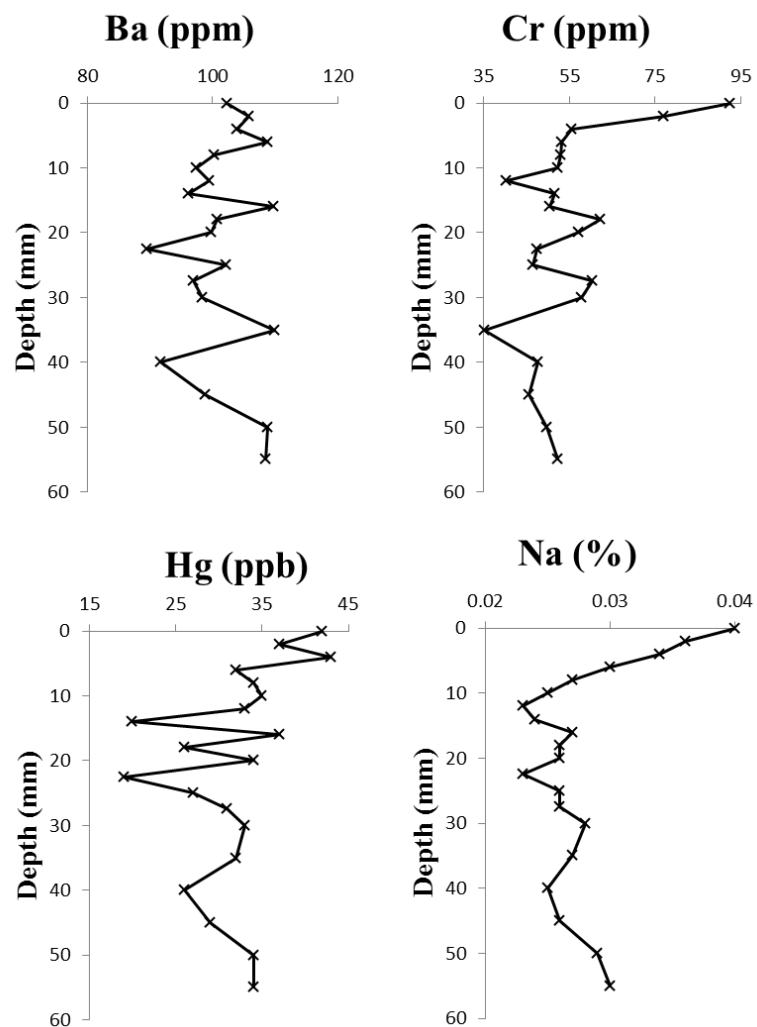


## Appendices

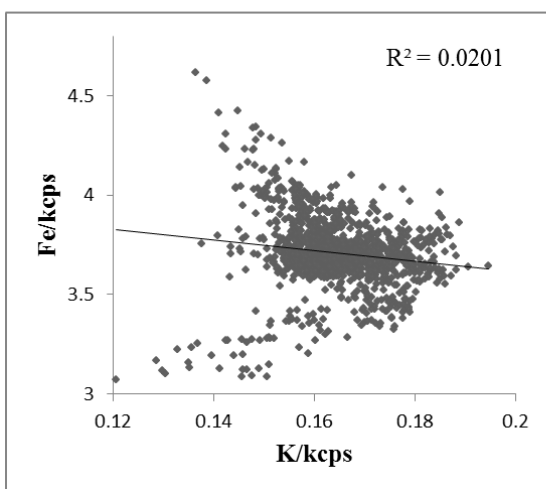
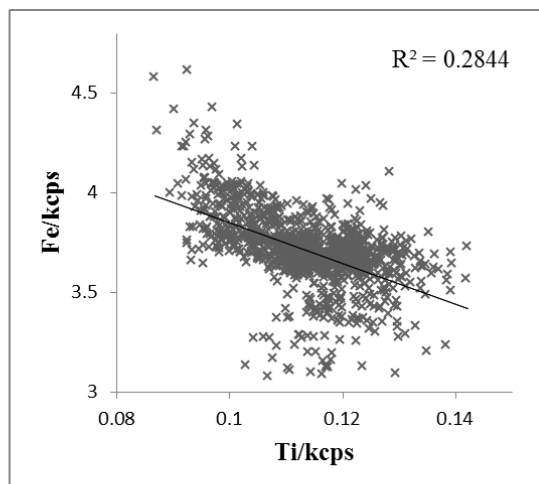
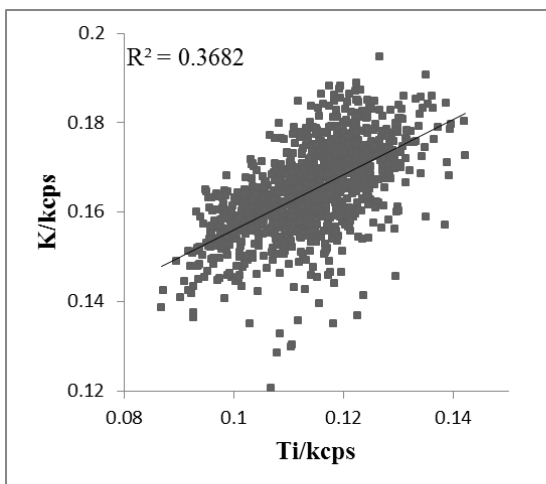
### Appendix A—Additional Figures



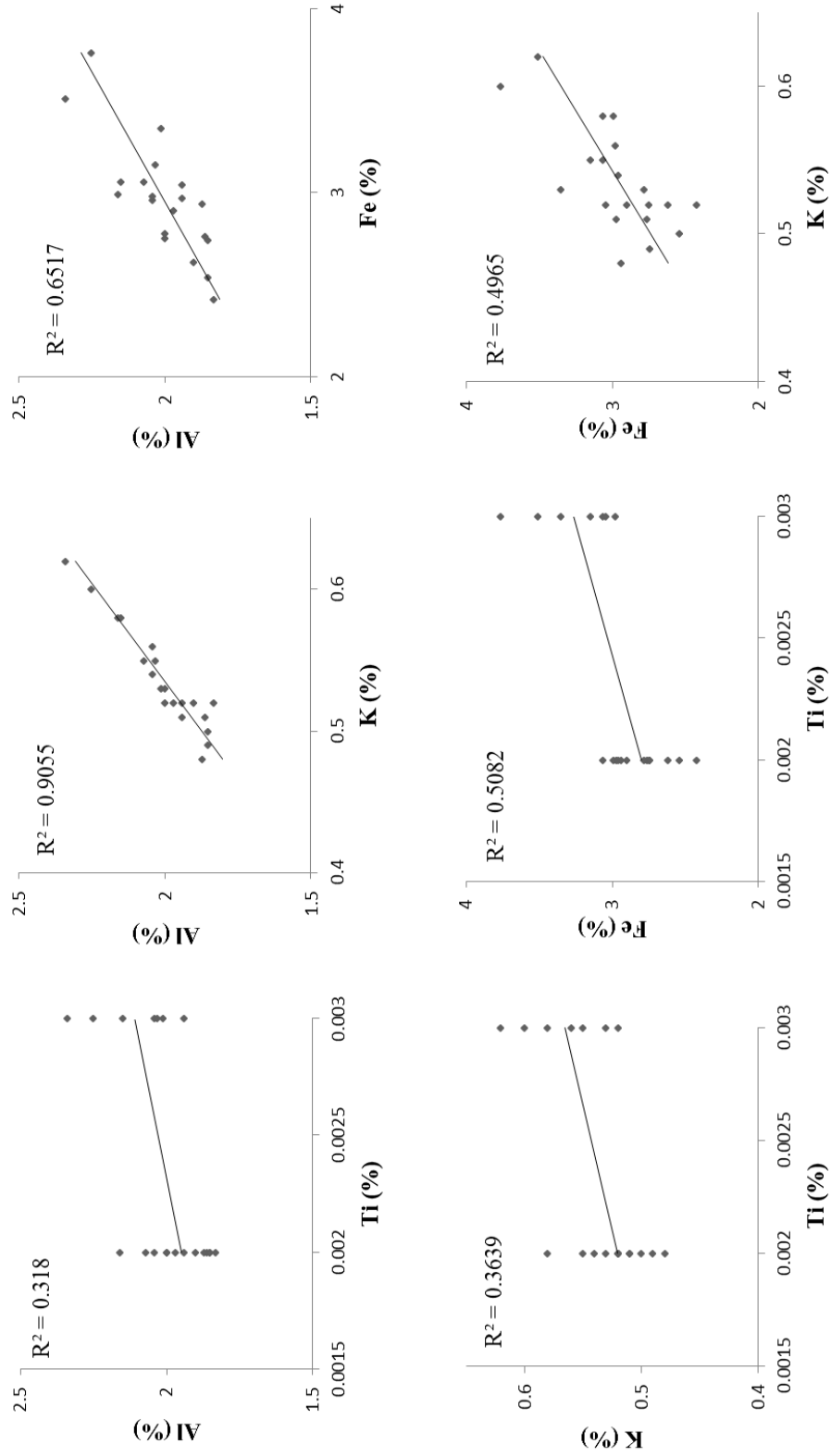
**A-1** Water mass fractions of core D10.5 subsamples collected for chronostratigraphic techniques. Differences among subsamples of similar depth in the upper 10.8cm are likely the result of drying between earlier subsampling (gray with x's) and later subsampling (black with circles).



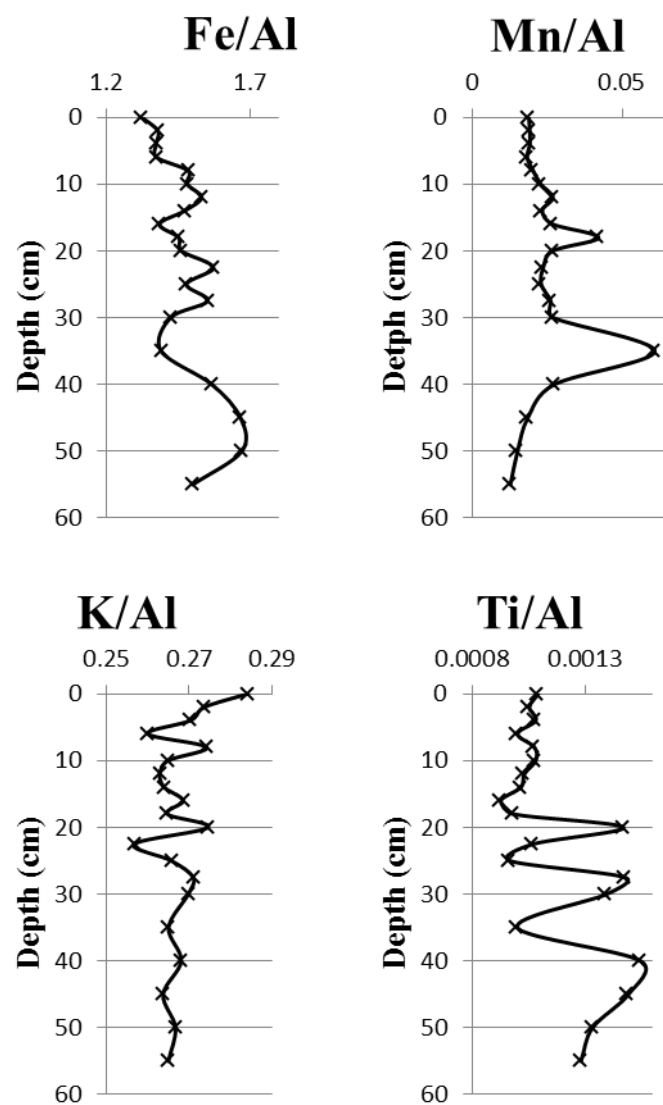
**A-2** Geochemical profiles of the elements Ba, Cr, Hg, and Na for core D10.5, measured with inductively coupled plasma mass spectrometry.



**A-3** Scatterplots of various pairings of K, Fe, and Ti ITRAX X-ray fluorescence data, with linear regressions plotted and corresponding r-values presented. Values represent peak area normalized by kilocounts per spectrum (kcps).



**A-4** Scatterplots of various pairings of Al, Fe, K, and Ti inductively coupled mass spectrometry data, with linear regressions plotted and corresponding r-values presented.



**A-5** Al-normalized profiles of Fe, Mn, K, and Ti for core D10.5, measured with inductively coupled plasma mass spectrometry.

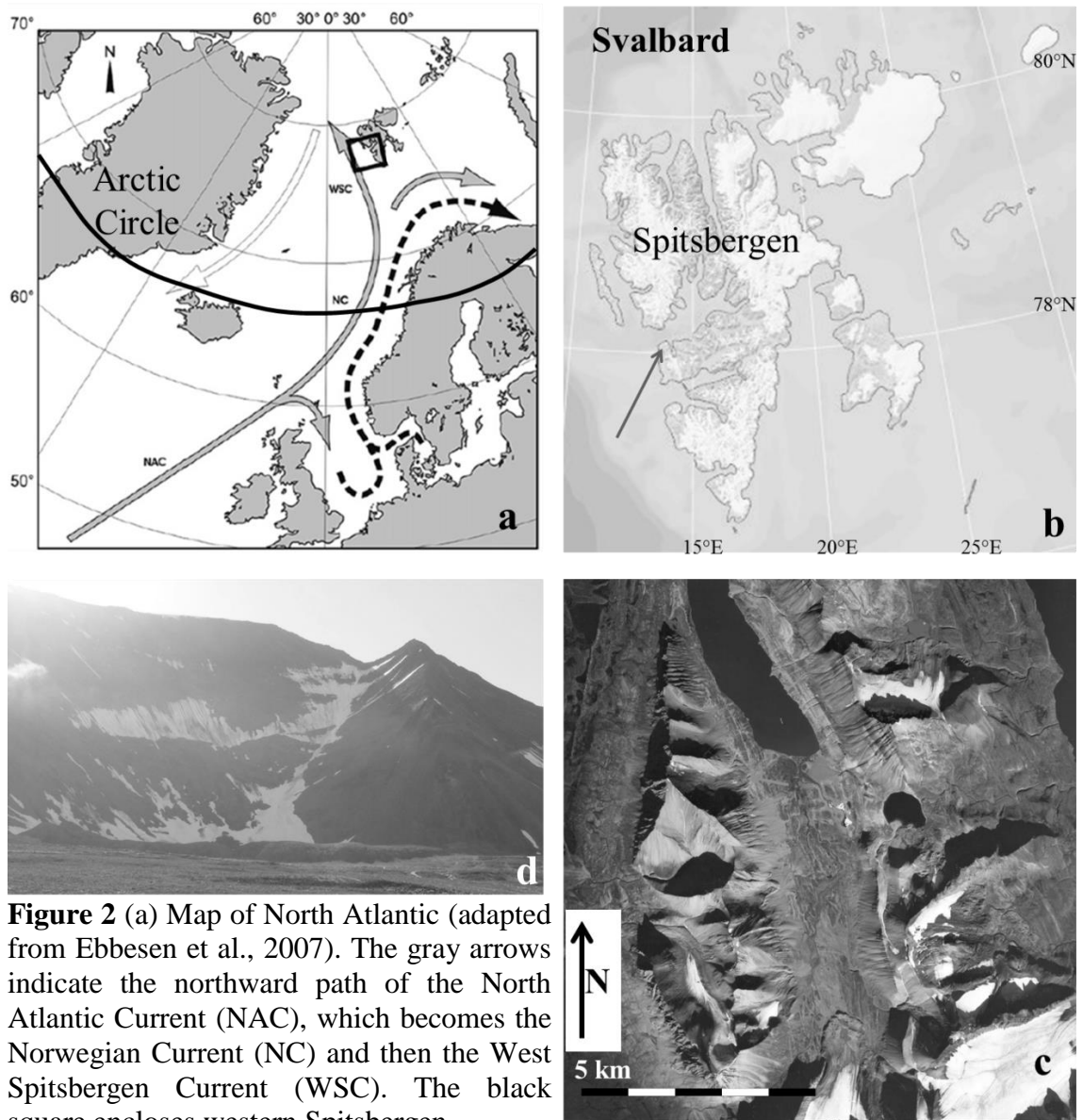


**Figure 2** (a) Map of North Atlantic (adapted from Ebbesen et al., 2007). The gray arrows indicate the northward path of the North Atlantic Current (NAC), which becomes the Norwegian Current (NC) and then the West Spitsbergen Current (WSC). The black square encloses western Spitsbergen.

(b) Map of the Svalbard archipelago with the field site indicated by a red arrow (adapted from [www.toposvalbard.nopolar.no](http://www.toposvalbard.nopolar.no)). (c) Vertical aerial photograph of Linnédalen. Location of west basin cirque is indicated by a yellow arrow (adapted from 1995 aerial photograph; Norsk Polarinstitutt). (d) Photograph of the west basin cirque and moraine. Yellow arrow in (c) indicates position of the photographer.

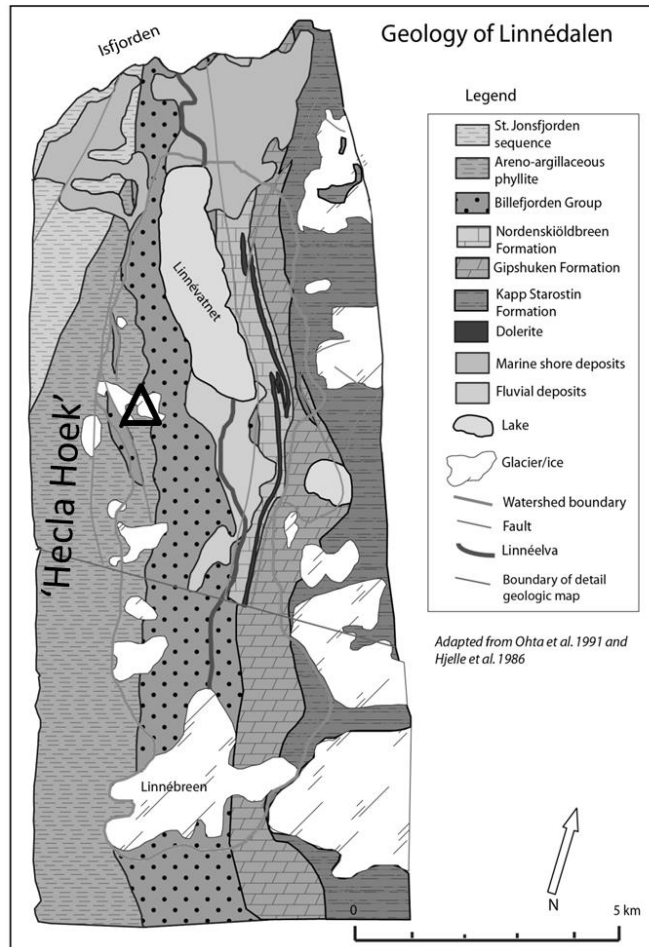


**Figure 2** Bedrock geologic map of Linnédalen. Purple units are the low-grade Lågneshukta metapelites of the Hecla Hoek complex, the blue Billefjorden Group consists of conglomerates and coal-rich sandstones, and the green units are carbonates of the Gipsdalen and Tempelfjorden Groups. A black triangle indicates the location of the west basin cirque. Figure adapted from Perreault (2006).

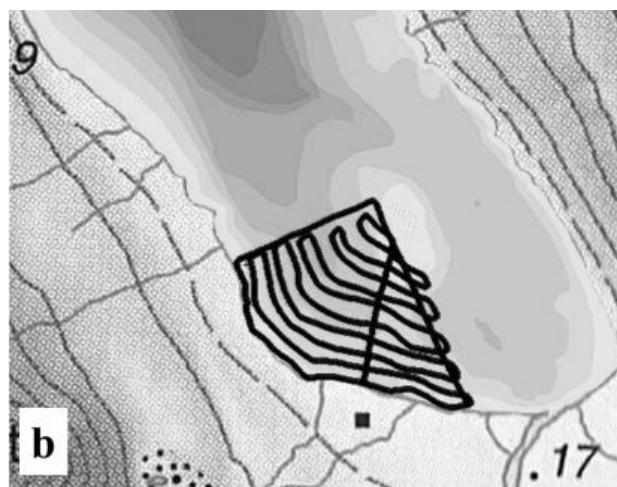
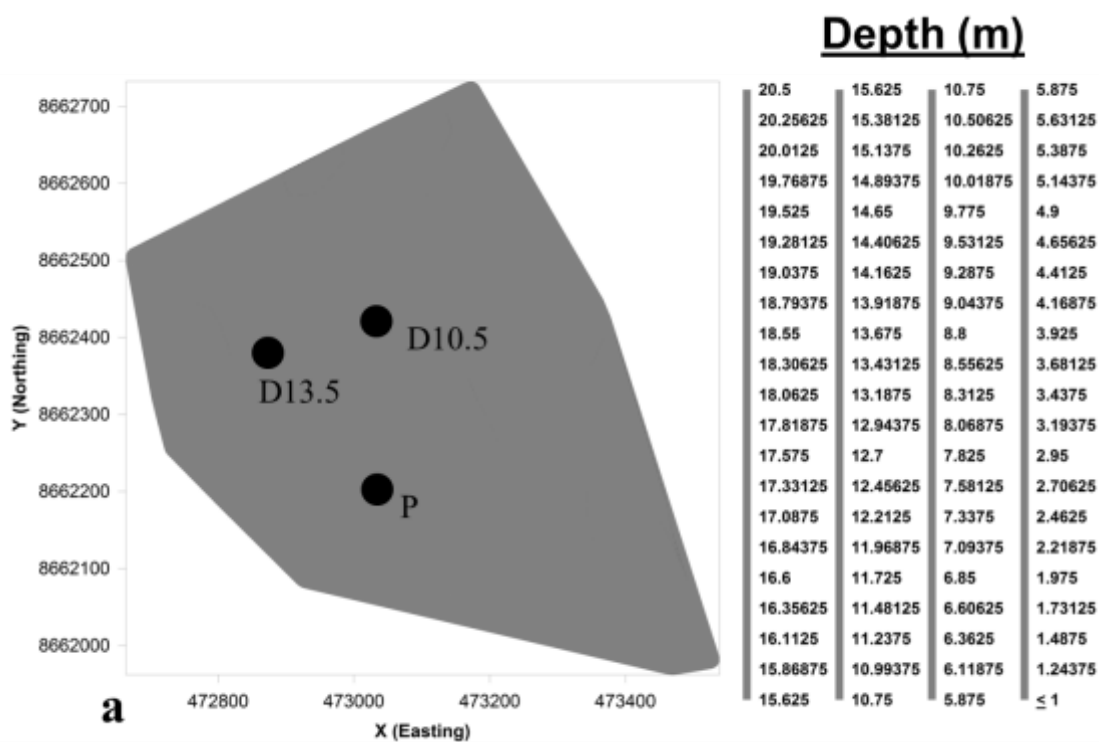


**Figure 3** (a) Bathymetric map of the Linnévatnet west basin, plotted in DPlot from bathymeter data, with location of core sites indicated. The contour scale indicates depth in meters. (b) Tracks over which bathymeter data was collected. Both images are adapted from maps plotted by Steven Roof, Hampshire College.



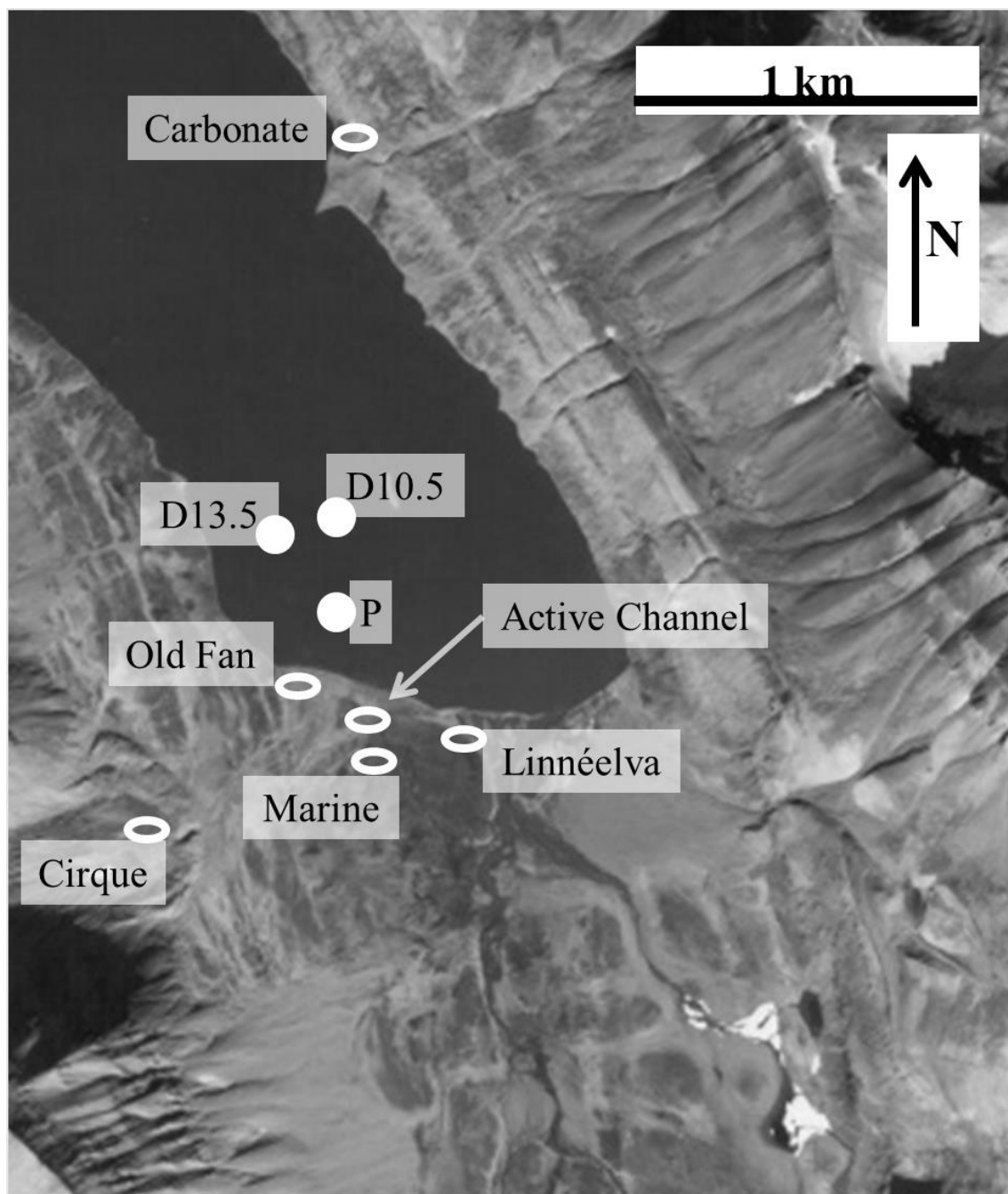


**Figure 4** Aerial photograph (1995; Norsk Polarinstitutt) of Linnévatnet's southern shore with sample site locations indicated. Lake sediment core sites are represented by white circles, while surficial sediment sample sites are represented by open ovals.

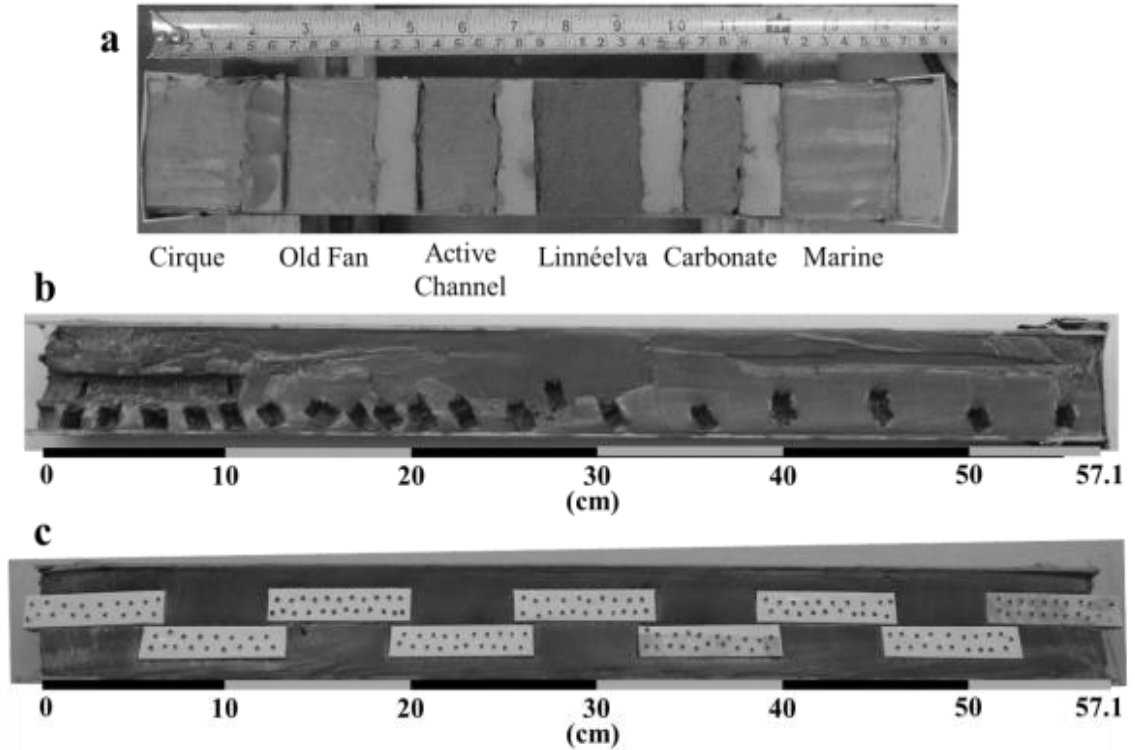


**Figure 5** Images of various core preparation and laboratory methods. (a) Artificial core with different sediment sources indicated. The green intervening regions are floral foam. Note that this image is not to scale with Figs. 5b and 5c. (b) Core D10.5 half used for chronostratigraphic subsampling. The region continuously sampled for  $^{239+240}\text{Pu}$ -based dating can be seen in the central upper 10cm, and variable interval sampling for chemostratigraphy can be seen down the entire core length. Stratigraphic up is oriented to the left. (c) Core D10.5 half used for thin-section subsampling. Note that the trays overlap adjacent trays or sediment edge by at least 1cm. Stratigraphic up is oriented to the left.

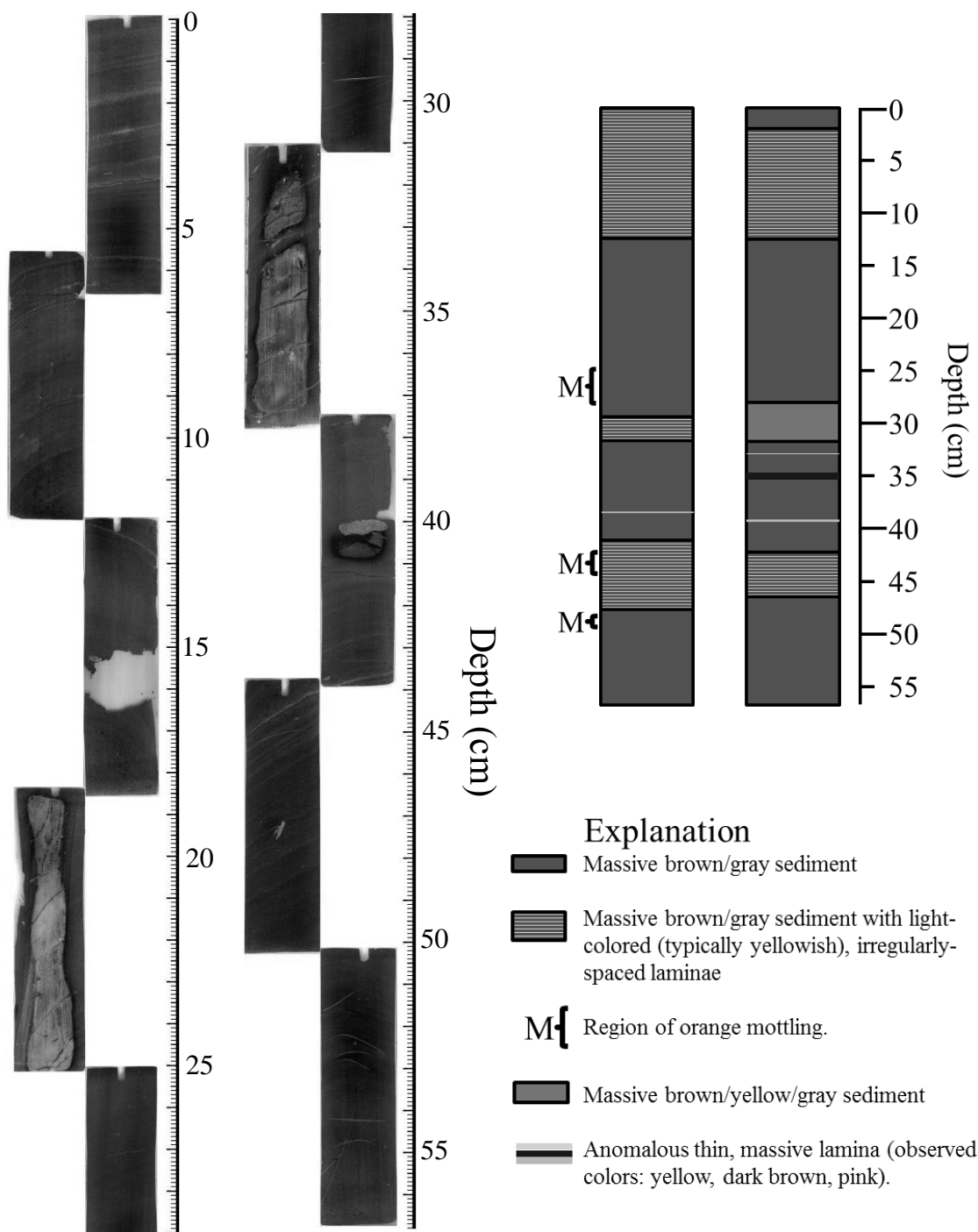


**Figure 8** Reconstruction of core D10.5 from aligned, thin-sections (digital scans with enhanced contrast) and stratigraphic logs of core D10.5 derived from microscopic analysis of thin-sections (I) and visual observations of the split-core surface (II). Pink layers in I and II are identical and the individual yellow laminae in II corresponds with the base of the middle laminated region in I. The dark layer observed in II was not observed in thin-section. Orange mottling observed in I is superimposed upon the texture of the sediment.

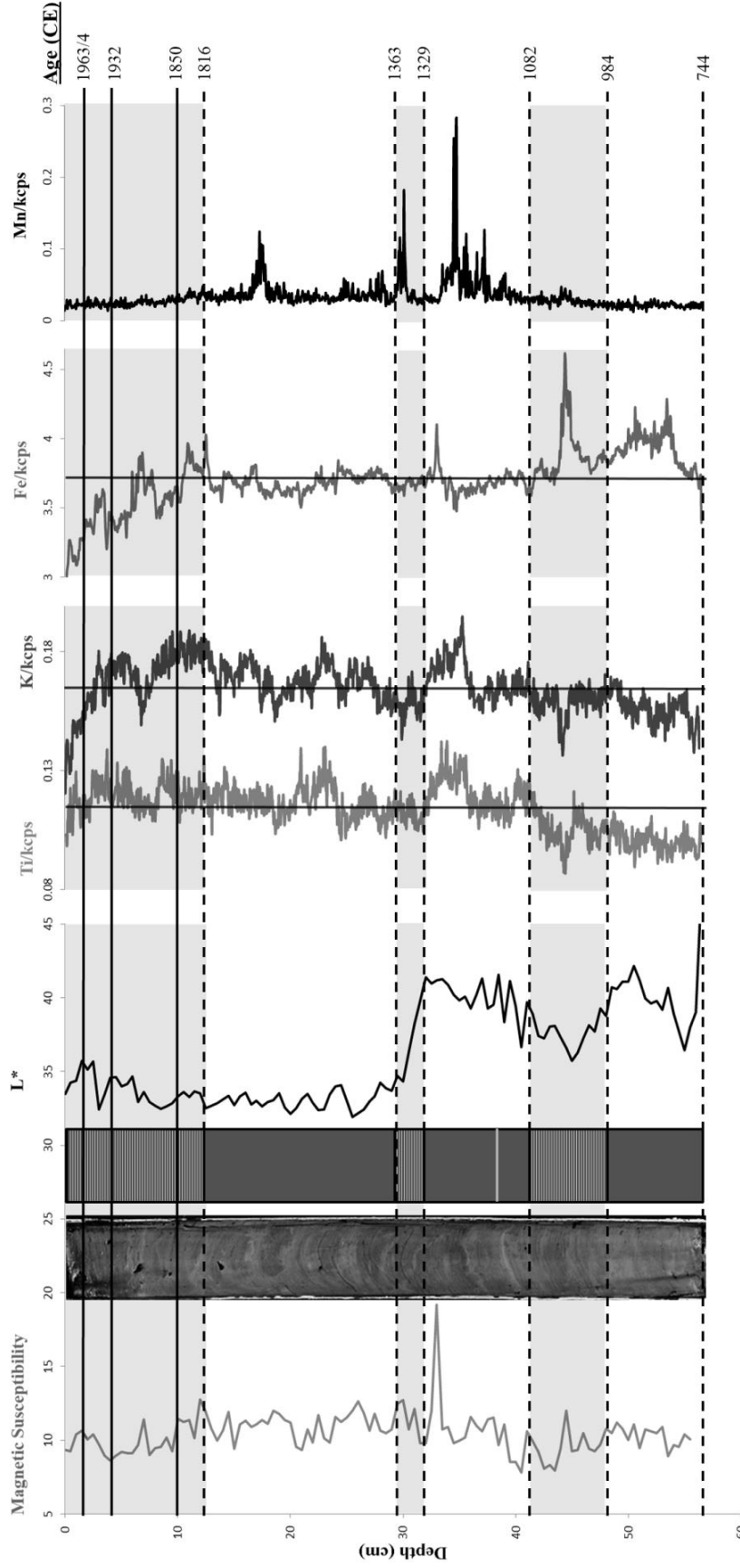


**Figure 10** Geochemical and physical parameter profiles of core D10.5. The dimensionless parameters magnetic susceptibility ( $\kappa$ ) and colorimetric lightness ( $L^*$ ) are measured at 5mm intervals. XRF profiles of Ti, K, Fe, and Mn are measured at 500 $\mu$ m intervals, and values represent peak area normalized by kilocounts per spectrum (kcps). Vertical lines superimposed on profiles of Ti, K, and Fe represent whole-core means. Shaded areas represent portions of core with abundant light-colored laminae. An enhanced-contrast image and thin-section-based stratigraphic log (see Fig. 8) of core D10.5 are shown for reference. Solid black lines represent absolute ages based upon  $^{239+240}\text{Pu}$  radionuclide dating (1963/64) and chemostratigraphic dating (1932, 1850 CE), while dashed lines represent ages calculated from sedimentation rates (see Fig. 9).

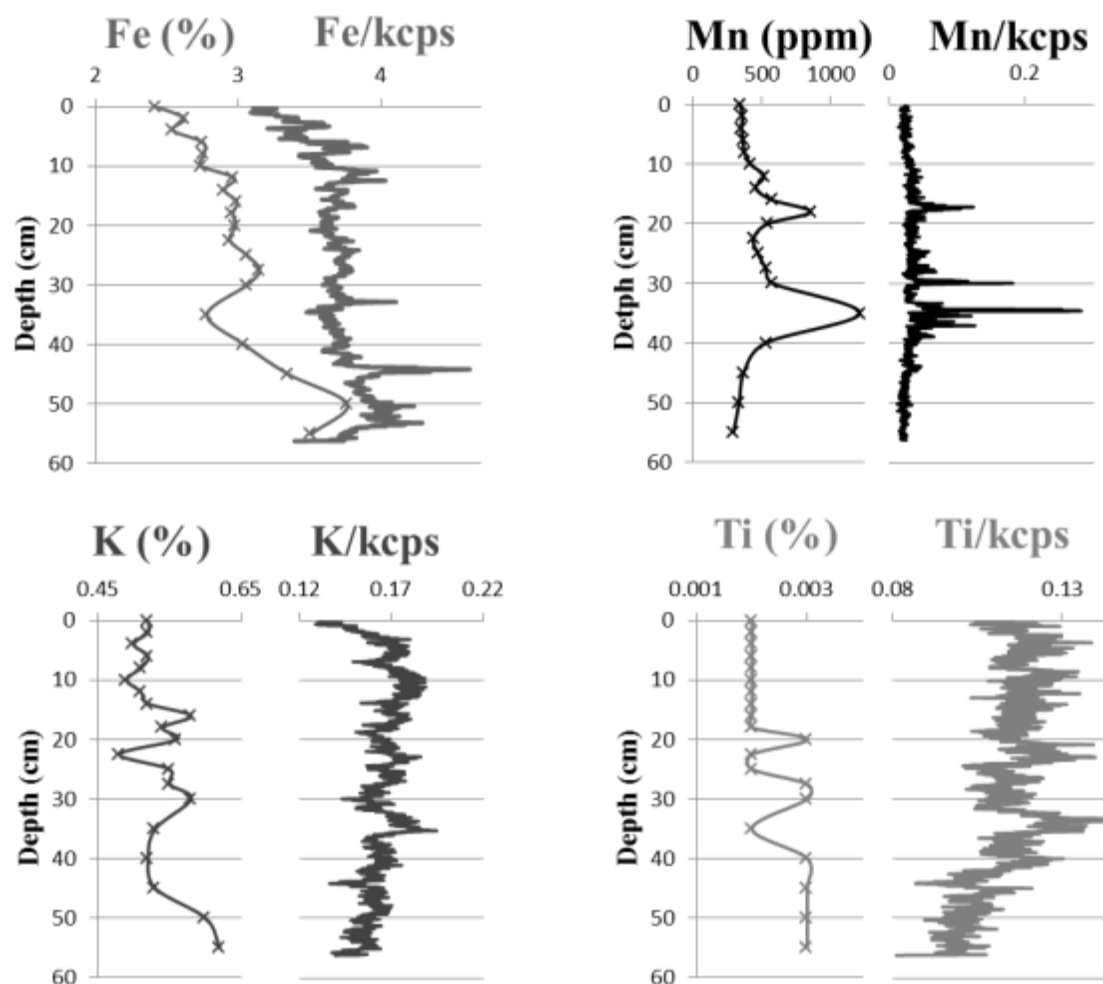


**Figure 11** Comparison of XRF data (continuous curves) and ICP-MS data (x's) from core D10.5, plotted as a function of depth, for the elements Fe, Mn, K, and Ti. ICP-MS data are measured as proportions of sample mass, while XRF data is measured in peak area and normalized by kilocounts per spectrum (kcps). Large scale patterns are in agreement between XRF and ICP-MS data for Fe and Mn, but not between XRF and ICP-MS data for K and Ti.

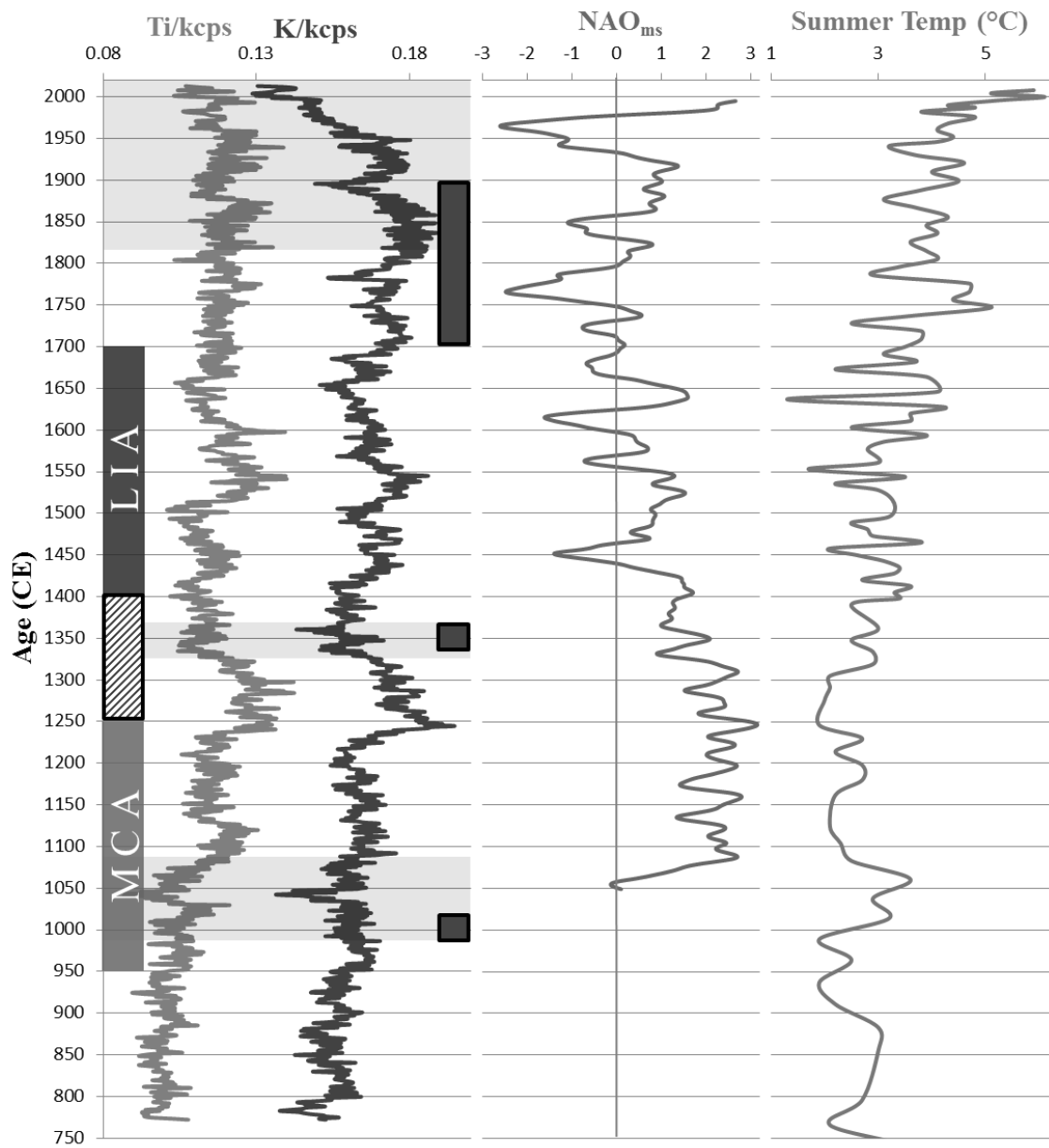


**Figure 12** Profiles of XRF-measured K and Ti (measured in peak area and normalized by kilocounts per spectrum) plotted against the age-model of core D10.5, with intervals of abundant, light-colored laminae indicated by the shaded regions. Superimposed on the K/kcps and Ti/kcps plot are periods of moraine stabilization on Spitsbergen (teal rectangles; Werner, 1993), as well as the duration of the Medieval Climate Anomaly (MCA), Little Ice Age (LIA), and intervening transitional period (box with horizontal bars), as described by Mann et al. (2012). The transitional period is typically associated with early LIA conditions (e.g. Grove, 1988). Plotted for comparison are the winter NAO index reconstruction (green) of Trouet et al. (2009) and the Kong-B June-July-August air temperature reconstruction for Kongressvatnet (orange; D’Andrea et al., 2012).